Biogenesis of Mercury–Sulfur Nanoparticles in Plant Leaves from Atmospheric Gaseous Mercury

Alain Manceau, Jianxu Wang, Mauro Rovezzi, Pieter Glatzel, Xinbin Feng

▶ **To cite this version:**

Alain Manceau, Jianxu Wang, Mauro Rovezzi, Pieter Glatzel, Xinbin Feng. Biogenesis of Mercury–Sulfur Nanoparticles in Plant Leaves from Atmospheric Gaseous Mercury. Environmental Science and Technology, 2018, 52 (7), pp.3935-3948. 10.1021/acs.est.7b05452 . hal-02314769

HAL Id: hal-02314769
https://hal.science/hal-02314769v1

Submitted on 13 Oct 2019

HAL is a multi-disciplinary open access archive for the deposit and dissemination of scientific research documents, whether they are published or not. The documents may come from teaching and research institutions in France or abroad, or from public or private research centers.

L'archive ouverte pluridisciplinaire **HAL**, est destinée au dépôt et à la diffusion de documents scientifiques de niveau recherche, publiés ou non, émanant des établissements d'enseignement et de recherche français ou étrangers, des laboratoires publics ou privés.

Biogenesis of Mercury-Sulfur Nanoparticles in Plant Leaves from Atmospheric Gaseous Mercury

Alain Manceau,*,† Jianxu Wang,‡ Mauro Rovezzi,§ Pieter Glatzel,§ Xinbin Feng*,‡

†ISTerre, Université Grenoble Alpes, CNRS, CS 40700, 38058 Grenoble, France

‡State Key Laboratory of Environmental Geochemistry, Institute of Geochemistry, Chinese Academy of Sciences, Guiyang 550081, People's Republic of China

§European Synchrotron Radiation Facility (ESRF), 71 Rue des Martyrs, 38000 Grenoble, France.

*To whom correspondence should be addressed. E-mail: alain.manceau@univ-grenoble-alpes.fr; fengxinbin@vip.skleg.cn

Contacts : Alain Manceau: +33 (0)4 76 63 51 93; Xinbin Feng: +86 851 85895728

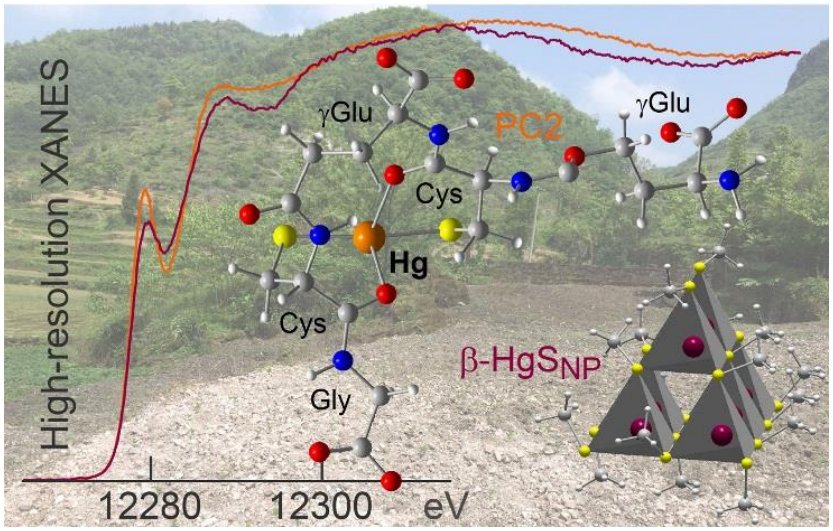

TOC

ABSTRACT: Plant leaves serve both as a sink for gaseous elemental mercury (Hg) from the atmosphere and a source of toxic mercury to terrestrial ecosystems. Litterfall is the primary

deposition pathway of atmospheric Hg to vegetated soils, yet the chemical form of this major Hg input remains elusive. We report the first observation of *in vivo* formation of mercury sulfur nanoparticles in intact leaves of 22 native plants from six different species across two sampling areas from China. The plants grew naturally in soils from a mercury sulfide mining and retorting region at ambient-air gaseous-Hg concentrations ranging from 131 ± 19 ng m^{-3} to 636 ± 186 ng m^{-3} and had foliar Hg concentration between 1.9 and 31.1 ng Hg mg^{-1} dry weight (ppm). High energy-resolution X-ray absorption near-edge structure (HR-XANES) spectroscopy shows that up to 57% of the acquired Hg is nanoparticulate, and the remainder speciated as a *bis*-thiolate complex ($Hg(SR)_2$). The fractional amount of nanoparticulate Hg is not correlated with Hg concentration. Variation likely depends on leaf age, plant physiology, and natural variability. Nanoparticulate Hg atoms are bonded to four sulfide or thiolate sulfur atoms arranged in a metacinnabar-type (β-HgS) coordination environment. The nanometer dimension of the mercury-sulfur clusters outmatches the known binding capacity of plant metalloproteins. These findings give rise to challenging questions on their exact nature, how they form, and their biogeochemical reactivity and fate in litterfall, whether this mercury pool is recycled or stored in soils. This study provides new evidence that metacinnabar-type nanoparticles are widespread in oxygenated environments.

INTRODUCTION

Plant foliage takes up gaseous elemental mercury (Hg^0_g) from the atmosphere. This is followed by litterfall or ingestion of leaves, so this is a primary deposition pathway on vegetated land and a main trophic source of mercury.[1-11] The chemical form this atmospheric mercury takes in leaf tissue is of both fundamental and practical interest. From the fundamental perspective, chelation and sequestration of metals by particular ligands is the molecular mechanism by which plants cope with metal stress. Therefore, knowing how mercury undergoes biotransformation is critical to understanding how it is detoxified in response to exposure. Given how toxic mercury is to biota, we also need to know in which form divalent mercury (Hg(II)) enters terrestrial ecosystems and is metabolically processed at the next trophic level by detritus feeders and herbivors. Practical

motivations include knowing how we can apply phytotechnology to remediate contamination,[12-17] and using plants (e.g., tree barks and lichens) for present and retrospective monitoring of airborne mercury.[18, 19]

The only available speciation study on natural leaves is for *Marrubium vulgare* (Horehound) from two Hg-polluted soils near a cinnabar (α-HgS) mining site in Spain. There the leaf Hg concentration was 61 and 183 ng Hg mg^{-1} dry weight (ppm dwt).[20] Cinnabar, metacinnabar (β-HgS), and a Hg-biothiol complex (Hg-SR) were identified using L_3-edge extended X-ray absorption fine structure (EXAFS) spectroscopy. The two sulfide minerals were considered to be soil microparticles deposited on the leaves. Thiol sulfur Hg-binding ligands, interpreted as cysteine residues, were also identified from *ex situ* experiments with added mercury.[20, 21] Phytochelatins (PCn = $(\gamma Glu\text{-}Cys)_n$-Gly), which are oligomers of glutathione (GSH = γGlu-Cys-Gly) that mediate metal detoxification,[22-25] are the only mercury ligands that have been characterized chemically, also with added mercury, using high-performance liquid chromatography coupled to high-resolution mass spectrometry (HPLC-MS).[26-28] Mercury complexes with PC2 and PC3 were identified in leaves of *Arabidopsis thaliana* exposed to thirty micromolar $HgCl_2$ for one and two days yielding an uncommonly high leaf content of 400 ng Hg mg^{-1} dwt.[29] No Hg-PC complex was detected at the environmentally relevant leaf content of 15-20 ng Hg mg^{-1} dwt with three micromolar $HgCl_2$, and no metal-PC complex has been identified to date in plants grown in the wild.

Absolute identification of the exact forms of metals occurring naturally in plant tissues, cells, and organelles remains a major analytical challenge. While HPLC-MS is excellent at molecular characterization of chemically extractable species, it is difficult to conserve the *in vivo* species in the plant extract during sample preparation and analysis.[28, 30-32] Also, mass spectrometric analyses detect soluble biomolecules, not biominerals.[33] In contrast, with X-ray absorption spectroscopy such as EXAFS and X-ray absorption near-edge structure (XANES), we can quantify mixed organic and inorganic forms directly on the solid,[34, 35] although with lower sensitivity to molecular identity and elemental concentration than HPLC-MS. Typically, X-ray techniques provide the

bonding environment(s) of the metal with a current bulk detection limit for mercury in plants of about 10 ng mg^{-1} dwt for XANES and 50 ng mg^{-1} dwt for EXAFS.[17, 19-21, 36-42] In most cases, well-crystallized mineral species, such as α/β-HgS, can be differentiated, but Hg complexes with similar coordination cannot. Moreover, the chemical nature of the complexing molecule cannot be obtained unambiguously because the structural information is local, being limited to about 5 Å beyond the metal atom of interest.

To collectively tackle detection limit, sensitivity to mercury coordination, and insight into the nature of the complexing molecule, we applied a four-pronged approach. First, we collected leaves from 22 plants from the heavily mined Guizhou province in southwest China,[5] where the concentration of total elemental gaseous mercury commonly exceeds 50 ng m^{-3} in ambient air and typically reaches several tens of μg m^{-3} near artisanal mercury smelters.[8, 43] It has been estimated that emissions of Hg from this region to the global atmosphere accounted for 12% of the world total anthropogenic emissions.[44] The unique collection of plant leaves comprises eight *Pteris vittata* ferns (7.6 ng mg^{-1} < [Hg] < 31.1 ng mg^{-1}), two flowering plants (4.5 and 12.5 ng Hg mg^{-1}), ten shrubs (4.4 ng mg^{-1} < [Hg] < 30.2 ng Hg mg^{-1}), and two trees (1.9 and 4.9 ng Hg mg^{-1}). Second, we developed a new high-luminosity multi-analyzer spectrometer for measuring XANES spectra at high energy-resolution (HR-XANES) in environmental inorganic and biological systems down to, and below, the ppm Hg level.[45] The capability of this new instrument, demonstrated earlier for the characterization of mercury binding in scalp hair,[46] is documented here for the first time on plants. The gain in spectral resolution provides superior distinction of C, N, O, and S ligands.[46-48] Third, we built a large spectral database of mercury minerals and coordination complexes against which to compare the leaf HR-XANES spectra. Fourth, the geometries of mercury-cysteine clusters were computed at a high level of molecular orbital theory to help in distinguishing biothiol from mercury sulfide forms.

The article describes our work as follows. First, we present the concentrations of Hg^0_g in ambient air and total Hg in the 22 plants and in two plants grown in chambers with controlled Hg^0_g levels.

Next we determine the particulate forms of mercury in the mined ore and surrounding soils, which may come into contact with the leaf tissues based on comparing HR-XANES spectra and linear combinations of reference spectra.[34] Then we derive the variability of the Hg chemical forms among the leaves from the variance in the HR-XANES dataset as determined by principal component analysis (PCA).[49] We show that the complete set of leaf spectra can be described statistically with only three abstract components, interpreted to indicate that three distinct chemical forms are dominant. Two of the three forms are dithiolate complexes ($Hg(SR)_2$), one being new, and the third form is a multinuclear cluster of Hg(II) and sulfur atoms. We calculate the fractional amount of each Hg form in leaves by fitting linear combinations of spectra representing the pure Hg species to the dataset. Lastly, we discuss the nature of the multinuclear Hg species, a Hg(II)-cysteinate complex of plant metallothionein ($Hg_x(Cys)_y$) or a nanosized mercury sulfide mineral, and add complementary structural and molecular insights from first-principles calculations.[50-53]

MATERIALS AND METHODS

Materials. A detailed description of the Wuchuan and Wanshan sampling sites from the Guizhou province, Hg^0_g exposition experiment, mercury chemical analysis, and samples preparation for HR-XANES measurment is given in Supporting Information (SI). The HR-XANES spectra from the Hg ore, soils, and plant leaves were analyzed against a large spectral database of mercury minerals (α-HgS, β-HgS, nanosized β-HgS), Hg(II) complexes on natural organic matter (Hg-NOM), and Hg(II) and methylmercury (MeHg) model complexes with thiolate ligands.[46, 47, 53] This database was completed for this study with Hg(II) complexed to L-GSH (γ-Glu-Cys-Gly, M_m = 307.3; CAS = 70-18-8; Sigma-Aldrich), phytochelatin (PC; GeneCust Europe), metallothionein (MT), and the zwitterionic thiol ligand TabH (4-(trimethylammonio)benzenethiol).[54]

HR-XANES Spectroscopy. All Hg L_3-edge HR-XANES spectra were measured in high energy-resolution fluorescence yield detection mode with high-luminosity analyzer crystals[45] on

beamline ID26 at the European Synchrotron Radiation Facility (ESRF). Detailed information on data acquisition and analysis is given in the SI.

Computational Methodology. Geometry optimization of Hg_xS_y clusters and Hg complexes were performed at the second-order Møller-Plesset perturbation theory (MP2[55]) level with ORCA 3.0.3[56] and a computational scheme tested previously on the modeling of the structure and stability of monomeric Hg−thiolate complexes.[46, 47, 52 , 53, 57]

RESULTS

Mercury concentration. Ambient air Hg^0_g concentrations are in the range of $143 \pm 41 \leq Hg^0_g \leq 432 \pm 122$ ng m^{-3} at the Wuchuan sampling sites and $131 \pm 19 \leq Hg^0_g \leq 636 \pm 186$ ng m^{-3} at the Wanshan sampling sites (Figure 1a and SI Table S1). These concentrations are well within levels reported previously in the two mining districts.[8, 43] Ore-roasting and soil re-emission of previously deposited mercury are the main local source of Hg^0_g.[8, 58] Ground-to-air fluxes are extremely variable. Spatial and temporal influences, such as proximity and Hg concentration at the point source (mine, soil, roasting site) and ore processing activity, and variation in Hg response to environmental variables and processes, such as photoreduction at the soil surface, can adequately account for the mean variations in measured Hg^0_g from site to site. Consecutive measurements of Hg^0_g at each sampling site for 20 to 30 min with a time resolution of 15 s show large standard variation of the mean values, even at a short time-scale, which supports this (SI Table S2).

Foliar Hg concentrations vary from 1.9 to 31.1 ng mg^{-1}, also without significant difference between the Wuchuan ($4.4 \leq Hg \leq 31.1$ ng mg^{-1}) and the Wanshan ($1.9 \leq Hg \leq 29.5$ ng mg^{-1}) sampling sites (Figure 1a and SI Table S1). To make a comparison with crops, Hg concentrations between 0.2 and 0.8 ng mg^{-1} were measured in cole and tobacco leaves from the Wuchuan mining area.[59] The lowest concentration was observed for the evergreen coniferous *Platycladus orientalis* (named Po2 where the number represents [Hg] in ppm) collected at Hg^0_g of 143 ± 41 ng m^{-3}, and the highest concentration for the *P. vittata* fern (Pv31) collected at Hg^0_g of 432 ± 122 ng m^{-3}. There

is no trend in foliar Hg concentration as a function of plant species, Hg^0_g, or sampling site (Figure 1a). Previous studies have linked the Hg level in foliar tissue of the same species to the age of the leaf,[10, 60-63] with concentration increasing steadily throughout the season and more rapidly during high photosynthetic activity.[64] This data was not measured due to time limitations and because our main objective was to survey the chemical forms of Hg among a large variety of plant species, not to examine how they evolved over time in any particular plant.

A sense of the extent of Hg loading with time is informed from *P. vittata* and *Zea mays* (corn) grown in a greenhouse at Hg^0_g concentration of 1000-1500 ng m^{-3} (SI). For *P. vittata*, foliar Hg concentration was 0.09 ng mg^{-1} before exposure, 0.12 ng mg^{-1} after 7 days, 0.57 ng mg^{-1} after 20 days, and 2.2 ng mg^{-1} after 28 days. For *Z. mays* it was 0.05 ng mg^{-1} initially, 0.07 ng mg^{-1} after 7 days, 0.52 ng mg^{-1} after 20 days, and 2.9 ng mg^{-1} after 28 days. *P. vittata* contained about 20 times as much Hg after 28 days as initially, and *Z. mays* about 60 times. The first plant accumulated on average over this period 0.07 ng Hg mg^{-1} per day, and the second plant 0.10 ng Hg mg^{-1} day^{-1}. These figures are consistent with those reported for *Triticum durum* (wheat) exposed to 5000 ng m^{-3} Hg^0_g.[65] Foliar Hg concentration was 0.02 ng mg^{-1} before exposure, 0.39 ng mg^{-1} after 12 h, 1.90 ng mg^{-1} after 7 days, and 4.95 ng mg^{-1} after 15 days. Mercury levels were approximately 100 times higher after 7 days and 250 times higher after 15 days than at the beginning of the experiment. The average daily loading was 0.32 ng Hg mg^{-1} day^{-1}. After correcting for the difference in Hg^0_g concentration in the previous and current experiments, and taking a factor of 5000 / 1250 = 4, the renormalized daily accumulation of Hg in the *T. durum* experiment was 0.32 / 4 = 0.08 ng Hg mg^{-1} day^{-1}. This accumulation rate falls within the range of the *P. vittata* and *Z. mays* rates. We must therefore consider the plant's vegetative development. This effect, compounded by interspecific physiological differences and changes in environmental factors, can explain the variability in Hg concentration observed in wild plants from the same species and the lack of discernible trends in the 22 leaf tissues (Figure 1a). We can dismiss a soil effect because ^{198}Hg isotopic measurements showed that inorganic mercury contained in roots is marginally translocated to aerial parts.[66]

Mercury speciation in ore and soils. The Hg ore and the Soil16 spectra were identified as being from pure Hg species (Figures 2a and 2b). The ore spectrum has a highly structured pattern in the top-edge region, characteristic of Hg-Hg pairs from a well-crystallized mineral. Good spectral match was obtained with cinnabar (α-HgS) (fit residual, NSS = 6.1×10^{-5}). The Soil16 spectrum also has modulations in the top-edge region, but with lower amplitudes, either because there are fewer Hg-Hg pairs (smaller grain size) or because the Hg-Hg distances are unequal (structural disorder). The best shape that best matched the reference database was obtained for nanoparticulate metacinnabar (β-HgS_{NP}[47]) (NSS = 8.4×10^{-5}). Soil44 and Soil88 are intermediate between Hg ore and Soil16, indicating that Hg(II) must be present as a combination of α-HgS and β-HgS_{NP} (Figure 3a). Soil88 is well described by a mixture of 45% ± 7% α-HgS and 55 ± 8% β-HgS_{NP} (NSS = 4.6×10^{-5}, Figure 3b and SI Table S3). The precision of a HgS species percentage was estimated to be equal to the variation of its best-fit value obtained for an increase of 30% of the optimal NSS value (see details in the Data analysis section and SI Table S3). The best fit to the Soil44 spectrum is obtained with 17% ± 10% α-HgS + 33% ± 28% well-crystallized β-HgS + 55% ± 22% β-HgS_{NP} (NSS = 3.0×10^{-5}, Figure 3d and SI Figure S1a). A two-component fit of Soil44 yields 26% ± 7% α-HgS + 73 ± 8% β-HgS_{NP} (NSS = 4.5×10^{-5}, Figure 3c). Owing to the nature of the least-squares fitting, NSS is almost always smaller for a three-component fit than for a two-component fit simply due to the increase in the number of variable parameters with three components. Here, inclusion of well-crystallized β-HgS provides a better description of the data, but obviously at the expense of the precision on each component species. Soil107 has a two-component fit residual higher than the other soils (NSS = 14.2×10^{-5}). The quality of fit is clearly not good (Figure 3e), so we attempted a three-component fit to the database spectra. Adding 9% elemental Hg (Hg^0_s) decreases NSS by 24% (NSS = 10.8×10^{-5}) (Figure 3f). Therefore, it is at least plausible that Hg^0_s adds something significant to the reconstruction. The sensitivity to this reference is good, however, because the Hg^0_s HR-XANES spectrum is extremely structured at liquid helium temperature (SI Figure 1b), in contrast to previous observation.[67]

Organically-bound mercury was tested with Hg(II) reacted for 15 hours with the Elliott Soil humic acid [International Humic Substances Society (IHSS), catalog no. 1S102H]. This reference features a dithiolate complex ($Hg(SR)_2$) in which Hg(II) is linearly coordinated to two proximal SR^- thiolates and to distant SRS thioethers (2+*k* coordination).[47, 53] The $Hg(SR)_2$ complex is typical of the form of Hg(II) in soil organic matter.[68, 69] The linear RS-Hg-SR coordination produces, at high energy-resolution, a sharp absorption feature at 12279 eV not observed in the soil spectra (SI Figure S2). Linear least-squares combination fits of the soil spectra show that this species makes up at most 13% of total Hg (SI Figure S2). Soluble Hg-containing phases, previously described in gold mine tailings,[70] are incompatible models with detection limits of 7% for the model compound $HgCl_2$ and 3% for $[Hg(H_2O)_6]^{2+}$ (SI Figure S2).

Nano β-HgS is the dominant phase in all soils. It is unlikely to result from the transformation of α-HgS dust particles because the α allotrope is the thermodynamically stable mercury sulfide form at ambient conditions. Metacinnabar is metastable and transforms over time into α-HgS in the absence of impurities.[71-73] In 2016, we verified this by re-measuring the HR-XANES spectrum of a pure β-HgS reference synthesized and measured in 2014[47] (SI Figure S3). The $\beta\text{-HgS}_{NP}$ mercury species may result from the deposition and oxidation of Hg^0_g followed by the formation of a $Hg(SR)_2$ complex with soil organic matter and its subsequent transformation into $\beta\text{-HgS}_{NP}$.[47, 57]

Mercury speciation in foliage. Principal component analysis (PCA) of the 22 native plants and the two plants exposed for 28 days to gaseous mercury in a growth chamber (corn C3 and *P. vittata* Pv2) shows that three abstract components are required to account for the variance in the dataset (SI Figure S4). Looking closely at the data and surveying the reference spectra, we found that two component species are present in a single form in the leaf spectra: one (Sp1) in *Desmodium sequax Wall* (Ds4) and corn (C3) leaves (Figures 1b and 4a), and a second (Sp2) in four *P. vittata* leaves (Pv14, Pv19, Pv25, Pv31). The Sp1 spectrum has HR-XANES features that most closely match the reference spectra for Hg-(Cysteine)$_2$ (abbreviated as $Hg(Cys)_2$), Hg-(Glutathione)$_2$ (abbreviated as $Hg(GSH)_2$), and Hg-Phytochelatin (abbreviated as Hg-PC2) complex, in which Hg(II) is bonded

almost linearly to two cysteinyl sulfur atoms (thiolate SR^- ligand) and laterally to one or two secondary nitrogen or oxygen atoms ($Hg[(SR)_2+(N/O)_{1-2}]$ coordination) (Figures 4b and 4d, SI Figures S5, S6, S7, and S8). Recently described primary coordination to nitrogen atoms[74] was evaluated with the $Hg(Histidine)_2$ complex. This ligand gives distinctive HR-XANES signal (SI Figure S9). The Sp2 spectrum shows a distinct signature on the second absorption peak at *circa* 12288.5 eV (Figure 4a): its amplitude is enhanced as observed when Hg is bonded linearly to aryl thiolate ligands (SI Figure S10). Linear coordination was expected in leaf tissues because it is the most common geometry in mercury chemistry and it occurs in biological systems in complexes with cysteine, peptides, and proteins.[46, 75-84]

The third spectral component is a combination of Sp1/Sp2 and β-HgS_{NP} (Figures 4a and 4c). Nano β-HgS is manifested in the trailing spectral region of Figure 4a as a shift to the left, similarly to the soil spectra (Figure 3a). This shift signifies longer Hg-ligand distances, and is observed typically when Hg is tetrahedrally coordinated to sulfur atoms as in β-HgS[46]. A polynuclear tetracysteinate complex ($Hg_x(Cys)_y$) of the type existing in metalloproteins, represented here by a metallothionein isolate from *Mytilus edulis* (MT2), is an incompatible model (Figure 5 and Discussion).

We identified mercury-sulfur Hg_xS_y clusters with a β-HgS_{NP}-type structure in 15 leaf samples from six plant species, and in amounts ranging from 12% to 57% ± 8% (Figure 1b and SI Table S1). Since total Hg concentration in leaves is between 2 and 30 ppm, and the two HgS_{NP} richest plants (55% HgS_{NP} in Vn6 and 57% in Po2) have only 1.9 ppm (Po2) and 5.6 ppm (Vn6) Hg in the form of β-Hg_{SN}, the amount of this species is too vanishingly small to be observed by electron microscopy even with a cutting-edge instrument. The multinuclear Hg_xS_y species always coexists with at least one of the two linear forms Sp1 and Sp2. In contrast to Hg_xS_y, Sp1 and Sp2 can occur in pure form. Four wild *P. vittata* plants out of eight total contain only Sp2 (Pv14, Pv19, Pv25, Pv31, Figure 1b). After 28 days exposure to Hg^0_g, greenhouse C3 contains only Sp1, like the wild Ds4 plant, and greenhouse Pv2 has both Sp1 and Sp2, like the wild Pv8 plant. The high consistency

between speciation results obtained *ex situ* on artificially exposed plants and on native plants supports our experimental approach and suggests that the β-HgS_{NP}-type species is a secondary species that appears after some period of time. Field-grown leaves were much older than 28 days as they were sampled at the end of the florishing season on September 30 and October 15, 2015. For example, the green foliage of *Pteris vittata* appears in April and was therefore five-month old when collected in October. The leaves from *Vitex negundo* were even older because this shrud is semi-evergreen, shedding foliage and producing new foliage almost simultaneously in December-April. Longer exposure to gaseous elemental mercury also led to higher mercury concentration in leaf,[61] despite the lower vapor Hg concentration in the field relative to that in the growth chamber (Table S1). When comparing Hg speciation between field-grown and chamber-grown leaf, one needs to consider that β-HgS_{NP} takes typically at least a week to nucleate and start growing.[47] This secondary species is difficult to detect in a growth experiment when the plant is continuously exposed to Hg^0_g. To detect fresly formed β-HgS_{NP}, one would need to stop evaporating Hg in the gas chamber to let the new added Hg atoms react with reduced sulfur.

DISCUSSION

A highlight of this study is the detection of mercury-sulfur clusters in leaves impacted by atmospheric contact with gaseous mercury. The origin and nature of the Hg_xS_y clusters can be apprised from their structure. Three hypotheses are examined below: (1) mercury sulfide grains from dust particles, (2) mercury-cysteinate clusters, and (3) cysteinate-protected mercury sulfide nanoparticles.

Mercury sulfide dust particles. If the Hg_xS_y clusters were acquired from dust fallout, one would expect the β-HgS_{NP} particles to be associated with α-HgS particles from the nearby mercury mines. With typical length of 20-30 μm and width of 10-20 μm,[85, 86] epidermal stomatal pores could allow the finest α-HgS grains to enter the leaf tissues. However, gravity would limit this contamination pathway because stomata are more numerous on the abaxial (hypostomatic) than on

the adaxial (epistomatic) leaf surface for most plant species.[85] Here, at least two plants containing Hg_xS_y are known to be hypostomatous, *P. vittata* and *Juglans regia*.[85, 86] Mineral particles on the upper leaf surface can also be dismissed because the leaves were carefully washed with purified water. Actually, an α-HgS particle was detected in one spot of *Vitex negundo* (Vn30) out of 108 spots measured for this plant (Figure 6). No α-HgS particles were detected in the 21 other wild plants, representing a total of 21 x 108 = 22268 points measured by HR-XANES. We conclude from this that the β-HgS_{NP}-type species has an endogenous origin.

Mercury-cysteinate clusters. A second possibility is the binding of Hg(II) to multi-metal binding sites of metalloproteins, such as metallothioneins (MTs). Metallothioneins are small cysteine-rich proteins considered to be involved in the homeostasis of essential metal ions (i.e., Zn(II) and Cu(I)), to confer metal resistance (e.g., Cd(II) and Hg(II)), and to scavenge cell damaging reactive oxygen species (ROS).[87-89] Stomata guard cells, which regulate gas exchange (CO_2, O_2, H_2O, Hg^0_g), contain numerous proteins harboring cysteine residues and conveying environmental signaling.[87, 90, 91]

Divalent Zn and Cd (hereafter referred to as Me^{II}) are bound to MTs mainly as tetracysteinate complex to terminal (μ-SR) and bridging (μ_2-SR) cysteinyl sulfur ligands. Mononuclear $Me^{II}(Cys_2His_2)$ complexes,[88, 92] and homometallic dinuclear $Me^{II}_2Cys_6$,[93, 94] trinuclear $Me^{II}_3Cys_9$,[88, 92] and tetranuclear clusters are known in plants[95, 96] (Figure 7). The structures of the three- and four-metal clusters are described below. The trinuclear plant cluster is isostructural to the $Me^{II}_3Cys_9$ cluster from the β domain of animal MTs, although plant and animal MTs differ in the number and distribution pattern of the Cys residues in the amino-acid sequence.[97-99] The three $Me^{II}(Cys)_4$ tetrahedra from the structurally conserved $Me^{II}_3Cys_9$ cluster are connected by apices via three cysteinyl sulfurs which each bridges only two Me atoms (μ_2-SR sulfur atoms) (Figure 7a). The same polyhedral connectivity exists in β-HgS, except that all bulk sulfur atoms are of the μ_4-S type (insert in Figures 2b and 7b).

A $Me^{II}_4Cys_{10}His$ amino acid composition was inferred for the *Musa acuminata* (banana)

306 tetranuclear cluster (Figure 7g).[95] It resembles the common $Me^{II}_4Cys_{11}$ cluster from the α domain
307 of animal MTs[97] with a Cys residue replaced by an histidine residue (Figure 7c),[95] and also the
308 $Me^{II}_4Cys_9His_2$ cluster in a cyanobacterial MT[100] with one of the two His residues replaced by one
309 Cys residue. The $Me^{II}_4Cys_{11}$-α cluster arrangement is obtained by bonding a fourth tetracysteinate
310 to two terminal μ_1-SR sulfurs from a $Me^{II}_3Cys_9$–β cluster. The *Mytilus edulis* MT reference (MT2)
311 used in this study has a prototypical $Me^{II}_3Cys_9$–β site and a Me^{II}-binding α site that differs little
312 from the $Me^{II}_4Cys_{11}$–α site. The α cluster arrangement in *M. edulis* is obtained by attaching a fourth
313 tetracysteinate to a β-type $Me^{II}_3Cys_9$ cluster by a single μ_1-SR sulfur[101] (Figure 7e). Consequently,
314 the stoichiometry of the Mytilidae α site is $Me^{II}_4Cys_{12}$ instead of $Me^{II}_4Cys_{11}$, common in animals.
315 The $\{Me^{II}_4Cys_{12}\}$ core of $Me^{II}_4Cys_{12}$-α can be represented as a portion of the β-HgS lattice, like
316 the $\{Me_3S_9\}$ core of $Me^{II}_3Cys_9$-β (Figures 7e and 7f). However, the $\{Me_4S_{11}\}$ core of $Me^{II}_4Cys_{11}$-
317 α cannot (Figures 7c and 7d). In a tetranuclear β-HgS-type cluster each tetrahedron shares three
318 sulfurs yielding an adamantane-type cage (Figure 7d). In $Me^{II}_4Cys_{11}$-α, only two tetrahedra have
319 three bridging sulfurs and the two other have two bridging sulfurs (Figure 7c).

320 Lastly, a cluster with nuclearity five (Hg_5Cys_{12}) has been suggested in *Cicer arietinum*
321 (chickpea) MT, based on Hg:Cys stoichiometric considerations.[102] The Hg_5Cys_{12} model consists
322 of two dinuclear complexes of $Me^{II}_2Cys_6$-type[93, 94] linked by a fifth Hg(II) ion (Figure 7h). This
323 assemblage features $\{HgS_4\}$ tetrahedra linked by edges, not by apices as in all structurally known
324 Me^{II}-MT clusters and observed here by HR-XANES. In addition, edge-linkage in complexes
325 $[Hg_2(SMe)_6]^{2-}$, $[Hg_2(SPh)_6]^{2-}$, and $[Hg_5(SePh)_{12}]^{2-}$ is weakly stable.[103, 104] The $Hg_2(SMe)_6]^{2-}$
326 complex was shown by Raman spectroscopy to dissociate in solution into mononuclear
327 $[Hg(SMe)_3]^-$ ions.[105]

328 HR-XANES results show that the β-HgS_{NP} reference is a much better structure model to the
329 multinuclear Hg_xS_y foliar species than the MT2 mussel reference, despite the similarity of the
330 $\{HgS_4\}$ tetrahedral arrangements in the two references (Figure 7). To gain further insight into the
331 reason for the suitability of the β-HgS_{NP} model and incompatibility of the MT2 model, the

structures of Hg_3Cys_9, Hg_4Cys_{11}, Hg_4Cys_{12}, and $Hg_4Cys_{10}His$ were optimized geometrically and compared to the polyhedral β-HgS structure. Cysteine was replaced by the model thiolate ligand methanethiolate (CH_3S^-), as in our previous computational studies.[46, 47, 52, 53, 57, 106] This substitution does not change, or only marginally changes, the Hg-S bond length, the geometry of the complex, and the effective atomic charge on the sulfur (-0.63 e vs. -0.65 e) and Hg (+1.18 e vs. +1.16 e) atoms (SI Figure S11). However, the predicted Hg-Hg distances and geometry will be somewhat affected in MTs by the enfolding protein backbone structure. This effect was not taken into account in the modeling. The energy-minimized models are shown in Figure 7. The calculated Hg-S distances of the four $Hg_x(Cys)_y$ clusters are identical (2.52 ± 0.06-0.08 Å) and close to crystallographic values for inorganic $Hg(SR)_4$ complexes (2.566 ± 0.047 Å)[107] and well-crystallized β-HgS (2.53 Å[108]). The nearest Hg shell distance (d(Hg-Hg_1)) in Hg_4S_{11} (4.13 ± 0.19 Å) and $Hg_4S_{10}His$ (4.07 ± 0.20 Å) coincides with that in β-HgS (4.14 Å), whereas it is significantly longer in the two other clusters (4.43 ± 0.05-0.10 Å). The calculated Hg-N bond length in $Hg_4S_{10}His$ is about 0.2 Å shorter than the Hg-S distance and the geometry of the {HgS_3N} site is trigonal pyramidal with S-Hg-N angles of 101.7° ± 8.0° and S-Hg-S angles of 116.0° ± 7.4°, compared to the canonic 109.5° bond angles in a regular {HgS_4} tetrahedron (SI Figure S12). Overall, the $Hg_x(Cys)_y$ clusters have local structures close or broadly similar to β-HgS. In this respect, both the β-HgS_{NP} and MT2 references can be regarded as computationally tractable analogues for modeling the Hg_xS_y clusters in leaves. Because it is not the result of a difference in coordination mode, we need to explain that the β-HgS_{NP} model is fit and the MT2 model unfit.

The sulfide β-HgS_{NP} and cysteinate MT2 models differ in two complementary ways. One is greater variation in the calculated Hg-Hg distances in MT clusters, being more pronounced with four (± 0.10-0.20 Å) than three (± 0.05 Å) metals (Figure 7). A more significant reason is the cluster size: MT nanoclusters with nuclearity of only three to four are vanishingly small compared to nanosized β-HgS particles; MT2 lacks any Hg-Hg pair beyond 7 Å. These two factors, structural disorder and reduced size, indistinguishably cause smearing of the HR-XANES features as a result

of losing the multiple scattering events of the photoelectron on the Hg shells. This effect is clearly seen on the MT2 spectrum when it is superimposed on the spectra from the two leaf samples Po2 and Vn6 which have the highest proportion of the β-HgS_{NP} component (57% and 55%, respectively, SI Table S1). The MT2 spectrum has a bell-shaped top edge with no modulation of the absorption signal, whereas the two leaf spectra present oscillations from long distance Hg-Hg pairs (Figure 4b). We attempted to determine the size of the Hg_xS_y clusters in plant leaves.

The β-HgS_{NP} reference was used previously to model the HR-XANES spectrum of ~3-5 nm β-HgS nanocrystals in natural organic matter (NOM).[47] The mercury sulfide clusters in NOM evolved from $Hg(SR)_2$ complexes under aerated conditions within days to weeks at mercury concentrations of several hundred ppm down to three ppm. We examined whether one of the leaf spectra could be matched with an aged Hg-NOM spectrum. Good qualitative agreement was obtained between *V. negundo* Vn30 and a soil organic matter reacted for 10 days with 200 ng Hg mg^{-1} dwt, in which 53 ± 6 mol % of the Hg is speciated as $Hg(SR)_2$ and 47 ± 6 mol % as β-HgS_{NP} (NSS = 6.6×10^{-5}, Figure 8a). This match suggests some degree of similarity between the nanoclusters in Hg-NOM and in foliar tissues, but gives us little information on their respective size, as explained below.

Lattice plane spacings corresponding to those of β-HgS have been imaged previously in single 3-5 nm nanocrystals from the Hg-NOM with high-resolution transmission electron microscopy (HRTEM) (insert Figure 8a).[47] However, the nanocrystallized grains imaged by HRTEM likely contain structural defects and, consequently, have a crystal domain size (i.e., "crystallinity") lower than their macroscopic grain size of ~3-5 nm. In contrast to HRTEM, X-ray absorption spectroscopy (XAS) is sensitive to the structural environment of all selectively excited atoms (here Hg), including those located within a domain, in domain boundaries, and at the grain surface. Mercury atoms exposed at the surface and in the interstices of crystal domains have fewer Hg-Hg pairs and unequal bond lengths relative to those in the inside. Thus, XAS cannot distinguish large disordered nanoclusters of ~3-5 nm from smaller, less distorted clusters.[109] HR-XANES's lack of sensitivity to cluster size is compounded if all the nanoparticles are not identical in size, shape, and

chemical composition, which is generally the case in natural materials. The 1 nm {β-Hg_7S_{16}} cluster represented in Figure 8b provides a sense of the reduction of the Hg-Hg coordination in a nanometer-sized β-HgS particle. The Hg-Hg coordination number is 4 in the first-shell (4.14 Å), 0.6 in the second (5.85 Å), 1.1 in the third (7.17 Å), and 0.3 in the fourth (8.28 Å), compared to 12, 6, 24, and 12, respectively, for an infinite lattice. Based on XANES calculations,[110, 111] we estimate that the leaf clusters have at least this average size.

From these considerations the finding emerges that the Hg_xS_y clusters from the plant leaves are relatively big, probably several nanometers in size as observed for gold and silver nanoparticles in *Medicago sativa* (alfalfa) and copper in wetlands plants.[112-116] The maximum Hg binding capacity of MTs depends on the number of Cys residues. This number is extremely variable in plants, ranging from typically ten to 17 per MT molecule.[98] Assuming that the plant MTs have enough structural plasticity to bring the Cys-rich regions into proximity for large cluster formation,[99, 117] the number of Hg atoms within a β-HgS-type MT cluster is at most seven, for a total of 16 Cys residues (Figure 8b). Based on the β-HgS structure, at least two additional Cys residues will be required to incorporate an eighth Hg atom, bringing the total number of Cys residues to 18. This number exceeds the binding capacity of a single plant's MT molecule. Intermolecular Cys-Hg-Cys bonding with exogenous Cys residues cannot be excluded in principle because dimeric forms of MTs exist in animals. In Mytilidae, MT dimers are transcriptionally induced from DNA following specific exposure to Cd(II), not to Zn(II) nor Cu(I), and are enriched in Cd relative to the monomeric form.[118-123] We conclude from this that the β-HgS_{NP}–type structure identified by HR-XANES could be a mercury-cysteinate cluster of approximate stoichiometry Hg_7Cys_{16}.

Mixed sulfide-cysteinate mercury clusters. A third structural possibility is a mixed Hg sulfide and Hg cysteinate cluster, made of a sulfide mineral core and outer cysteine residues from an encapsulating protein, as known in organometallic compounds and Fe_xS_y metalloenzymes.[124-129] In the iron-storage ferritin protein, metalloclusters in the inner cage surface serve as putative nucleation sites that facilitate the subsequent growth of a mineral core.[130-132] Formation of

polymetallic Hg(II) species from $Hg(SR)_2$ thiolate complexes with concomitant loss of the peptide structure has been reported in *de novo* peptide mimicking the chelating properties of metalloproteins.[133] Thiolate complexes with d^{10} metals, such as $5d^{10}$ Au(I) and $4d^{10}$ Ag(I), are common precursors in the (bio)synthesis of metal sulfide and metallic nanoparticles. Capping with inorganic thiolate ligands or association with scaffolding Cys-rich proteins helps stabilize the particles and control their size, shape and crystallinity.[113, 134-142] Furthermore, thermodynamic calculation shows that the stability of Hg_xS_y clusters increases with nuclearity.[53] Metallophilic attraction is explained at the atomistic level by relativistic effects.[143, 144]

According to this scheme, the Hg sulfide core could be formed *in vivo* from the reaction of $Hg(SR)_2$ peptide complex with hydrogen (mono)sulfide (H_2S/HS^-) generated enzymatically by L-Cys desulfhydrase.[145-147] This enzyme enhances Arabidopsis tolerance to Cd(II) stress through the catalytic desulfuration of L-Cys and induction of MTs genes expression.[148] Biogenesis of Hg sulfide clusters could also occur via a reaction analogous to the production of Fe-S clusters in Arabidopsis.[149] Sulfur is provided by a cysteine desulfurase which releases S from Cys that subsequently becomes incorporated during Fe-S cluster synthesis. Lastly, sulfide sulfur could also be produced chemically by a dealkylation reaction between two $Hg(SR)_2$ complexes.[47, 57] This reaction can be written:

$$RS{-}Hg{-}SR + RS{-}Hg{-}SR \rightarrow RS{-}Hg\text{-}S\text{-}Hg\text{-}SR + R{-}S{-}R$$

The 1:1 molar ratio of S to Hg in the growing HgS core, compared to 2:1 initially in $Hg(SR)_2$, is obtained by replication of the previous nucleation reaction according to:

$$RS{-}Hg\text{-}S\text{-}Hg\text{-}SR + x(RS{-}Hg{-}SR) \rightarrow RS{-}(HgS)_{x+2}{-}R + x(R{-}S{-}R)$$

To occur, both the enzymatic sulfidization and chemical dealkylation routes require that the Hg atoms "see" each other, a likelihood which should normally increase with Hg concentration. Actually, the leaf fraction of $\beta\text{-}HgS_{NP}$ does not correlate with the Hg content. Noteworthy is *P orientalis* Po2, which is both most diluted in Hg (1.9 ppm) and most enriched in $\beta\text{-}HgS_{NP}$ (57%, Figure 1b and SI Table S1). Lack of correlation could plausibly be attributed to anatomical and

physiological variability within and among species. For instance, the inflow of gaseous Hg is not homogenous on the leaf surface but varies with the density of stomata, which is about 370-500/mm^2 for *V. negundo*,[150], 258/mm^2 for *P. vittata*,[86] 183-335/mm^2 for *J. regia*,[85] and below 100/mm^2 for corn.[151] The bulk Hg concentration does not reflect how the mercury atoms are distributed at the cell level because mercury is accumulated near the stomata. In NOM, β-HgS_{NP} was also observed to nucleate at the somewhat low Hg concentration of 3 ppm (Manceau et al., in preparation). In this case, one main reason is the natural clustering of thiolate groups in compositionally heterogeneous and polyfunctional macromolecular NOM. In biota, metalloproteins can sense metals and form polynuclear clusters at extremely low concentrations.[152] For instance, the regulatory protein MerR encoded by the *mer* operon responds to nanomolar Hg(II) concentrations.[153] MerR is also selective and discriminates Hg(II) against other chemically similar d^{10} heavy metals, such as Zn(II), Cd(II), Ag(I), and Au(I), even at concentrations in these metals two to three orders of magnitude greater than that required for Hg(II) detection.[153]

In summary, the results presented here show that aerial gaseous mercury taken up by leaf tissues can be sequestered as divalent mercury-sulfur nanoparticles. This finding suggests interesting hypotheses and also brings up challenging questions. For instance, is mercury partially biomineralized in sulfide form, or is it clustered as mercury-cysteinate complexes in cysteine-rich biomolecules? Is one of the two forms more stable than the other, therefore less toxic? May either form be remobilized or revolatilized once deposited in litterfall, or are they recalcitrant to biogeochemical transformation? To date, conversion of thiol-bound Hg(II) to nanoparticulate β-HgS under ambient atmospheric conditions has been documented in natural organic matter[47] and suggested to occur in contact with bacteria.[147] These considerations, together with the close similarity between the spectra from organic matter containing 3-5 nm HgS nanocrystals and from some of the leaf tissue is extremely strong support for the presence of HgS_{NP} in the leaves. Therefore, this new study provides another evidence for the widespread occurrence of β-HgS_{NP} under aerated conditions. Perhaps nanoparticulate metacinnabar, regardless of its biotic or abiotic

origin, is a main source of the legacy mercury pool stored in soils.[58, 154]

ASSOCIATED CONTENT

Supporting Information is available free of charge

Detailed experimental accounts, Figures S1-S13, Tables S1-S3, Cartesian coordinates of the optimized Hg_xS_y clusters and Hg complexes, ascii data from a selection of HR-XANES spectra.

AUTHOR INFORMATION

Corresponding authors

alain.manceau@univ-grenoble-alpes.fr

fengxinbin@vip.skleg.cn

Notes

The authors declare no competing financial interest.

ACKNOWLEDGEMENTS

Support was provided to A.M by the French National Research Agency (ANR) under grant ANR-12-BS06-0008-01, to A.M., M.R., and P.G. by the ANR under Grant ANR-10-EQPX-27-01 (EcoX Equipex), to J.W and X.F by Chinese Academy of Sciences (QYZDJ-SSW-DQC005). The Froggy platform of the CIMENT infrastructure (ANR Grant ANR-10-EQPX- 29-01) provided computing resources and Pierre Girard his expertise in parallel scientific processing. M. Lanson and A. Lannes are thanked for the preparation of Hg complexes, and Paco Bustamante and Serge Pin for the preparation of the metallothionein reference.

REFERENCES

(1) Rea, A. W.; Keeler, G. J.; Scherbatskoy, T., The deposition of mercury in throughfall and litterfall in the lake champlain watershed: A short-term study. *Atmos. Environ.* **1996,** *30*, 3257-3263.

(2) Rea, A. W.; Lindberg, S. E.; Scherbatskoy, T.; Keeler, G. J., Mercury accumulation in foliage over time in two northern mixed-hardwood forests. *Water Air Soil Poll.* **2002,** *133*, 49-67.

(3) Biester, H.; Müller, G.; Schöler, H. F., Estimating distribution and retention of mercury in three different soils contaminated by emissions from chlor-alkali plants: part I. *Sci. Tot. Environ.* **2002,** *284*, 177-189.

(4) Ericksen, J. A.; Gustin, M. S., Foliar exchange of mercury as a function of soil and air mercury concentrations. *Sci. Tot. Environ.* **2004,** *324*, 271-279.

(5) Feng, X.; Qiu, G., Mercury pollution in Guizhou, Southwestern China - An overview *Sci. Tot. Environ.* **2008,** *400*, 227-237.

(6) Meng, B.; Feng, X. B.; Qiu, G. L.; Cai, Y.; Wang, D. Y.; Li, P.; Shang, L. H.; Sommar, J., Distribution patterns of inorganic mercury and methylmercury in tissues of rice (*Oryza sativa* L.) plants and possible bioaccumulation pathways. *J. Agr. Food Chem.* **2010,** *58*, 4951-4958.

(7) Obrist, D.; Johnson, D. W.; Lindberg, S. E.; Luo, Y.; Hararuk, O.; Bracho, R.; Battles, J. J.; Dail, D. B.; Edmonds, R. L.; Monson, R. K.; Ollinger, S. V.; Pallardy, S. G.; Pregitzer, K. S.; Todd, D. E., Mercury distribution across 14 U.S. forests. Part I: Spatial patterns of concentrations in biomass, litter, and soils. *Environ. Sci. Technol.* **2011,** *45*, 3974-3981.

(8) Wang, J. X.; Feng, X. B.; Anderson, C. W. N.; Zhu, W.; Yin, R. S.; Wang, H., Mercury distribution in the soil-plant-air system at the Wanshan mercury mining district in Guizhou, Southwest China. *Environ. Toxicol. Chem.* **2011,** *30*, 2725-2731.

(9) Guédron, S.; Grangeon, S.; Jouravel, G.; Charlet, L.; Sarret, G., Atmospheric mercury incorporation in soils of an area impacted by a chlor-alkali plant (Grenoble, France): Contribution of canopy uptake. *Sci. Tot. Environ.* **2013,** *445*, 356-364.

(10) Assad, M.; Parelle, J.; Cazaux, D.; Gimbert, F.; Chalot, M.; Tatin-Froux, F., Mercury uptake into poplar leaves. *Chemosphere* **2016,** *146*, 1-7.

(11) Wang, X.; Bao, Z. D.; Lin, C. J.; Yuan, W.; Feng, X. B., Assessment of global mercury deposition through litterfall. *Environ. Sci. Technol.* **2016,** *50*, 8548-8557.

(12) Meagher, R. B.; Heaton, A. C. P., Strategies for the engineered phytoremediation of toxic element pollution: mercury and arsenic. *J. Ind. Microbiol. Technol.* **2005,** *32*, 502-513.

(13) Moreno, F. N.; Anderson, C. W. N.; Stewart, R. B.; Robinson, B. H., Mercury volatilisation and phytoextraction from base-metal mine tailings. *Environ. Poll.* **2005,** *136*, 341-352.

(14) Gardea-Torresdey, J. L.; Peralta-Videa, J. R.; de la Rosa, G.; Parsons, J. G., Phytoremediation of heavy metals and study of the metal coordination by X-ray absorption spectroscopy. *Coord. Chem. Rev.* **2005,** *249*, 1797-1810.

(15) Ruiz, O. N.; Alvarez, D.; Torres, C.; Roman, L.; Daniell, H., Metallothionein expression in chloroplasts enhances mercury accumulation and phytoremediation capability. *Plant Biotechnol. J.* **2011,** *9*, 609-617.

(16) Wang, J. X.; Feng, X. B.; Anderson, C. W. N.; Xing, Y.; Shang, L. H., Remediation of mercury contaminated sites - A review. *J. Hazard. Mater.* **2012,** *221*, 1-18.

(17) Wang, J. X.; Feng, X. B.; Anderson, C. W. N.; Wang, H.; Zheng, L. R.; Hu, T. D., Implications of mercury speciation in thiosulfate treated plants *Environ. Sci. Technol.* **2012,** *46*, 5361-5368.

(18) Grangeon, S.; Guedron, S.; Asta, J.; Sarret, G.; Charlet, L., Lichen and soil as indicators of an atmospheric mercury contamination in the vicinity of a chlor-alkali plant (Grenoble, France). *Ecol. Indic.* **2012,** *13*, 178-183.

(19) Chiarantini, L.; Rimondi, V.; Bardelli, F.; Benvenuti, M.; Cosio, C.; Costagliola, P.; Di Benedetto, F.; Lattanzi, P.; Sarret, G., Mercury speciation in *Pinus nigra* barks from Monte Amiata (Italy): An X-ray absorption spectroscopy study. *Environ. Poll.* **2017,** *227*, 83-88.

(20) Carrasco-Gil, S.; Siebner, H.; LeDuc, D. L.; Webb, S. M.; Millan, R.; Andrews, J. C.; Hernandez, L. E., Mercury localization and speciation in plants grown hydroponically or in a natural environment. *Environ. Sci. Technol.* **2013,** *47*, 3082-3090.

(21) Carrasco-Gil, S.; Alvarez-Fernandez, A.; Sobrino-Plata, J.; Millan, R.; Carpena-Ruiz, R. O.; Leduc, D. L.; Andrews, J. C.; Abadia, J.; Hernandez, L. E., Complexation of Hg with phytochelatins is important for plant Hg tolerance. *Plant Cell Environ.* **2011,** *34*, 778–791.

(22) Howden, R.; Goldsbrough, P. B.; Andersen, C. R.; Cobbett, C. S., Cadmium-sensitive, *cad1* mutants of *Arabidopsis thaliana* are phytochelatin deficient. *Plant Physiol.* **1995,** *107*, 1059-1066.

(23) Cobbett, C.; Goldsbrough, P., Phytochelatins and metallothioneins: Roles in heavy metal detoxification and homeostasis. *Annu. Rev. Plant Biol.* **2002,** *53*, 159-182.

(24) Clemens, S.; Kim, E. J.; Neumann, D.; Schroeder, J. I., Tolerance to toxic metals by a gene family of phytochelatin synthases from plants and yeast. *EMBO J.* **1999,** *18*, 3325-3333.

(25) Ha, S. B.; Smith, A. P.; Howden, R.; Dietrich, W. M.; Bugg, S.; O'Connell, M. J.; Goldsbrough, P. B.; Cobbett, C. S., Phytochelatin synthase genes from arabidopsis and the yeast *Schizosaccharomyces pombe*. *Plant Cell* **1999,** *11*, 1153-1163.

(26) Iglesia-Turino, S.; Febrero, A.; Jauregui, O.; Caldelas, C.; Araus, J. L.; Bort, J., Detection and quantification of unbound phytochelatin 2 in plant extracts of *Brassica napus* grown with different levels of mercury. *Plant Phys.* **2006,** *142*, 742-749.

(27) Chen, L. Q.; Yang, L. M.; Wang, Q. Q., *In vivo* phytochelatins and Hg-phytochelatin complexes in Hg-stressed *Brassica chinensis* L. *Metallomics* **2009,** *1*, 101-106.

(28) Krupp, E. M.; Mestrot, A.; Wielgus, J.; Meharg, A. A.; Feldmann, J., The molecular form of mercury in biota: identification of novel mercury peptide complexes in plants. *Chem. Comm.* **2009,** *28*, 4257-4259.

(29) Sobrino-Plata, J.; Carrasco-Gil, S.; Abadıa, J.; Escobar, C.; Alvarez-Fernandez, A.; Hernandez, L. E., The role of glutathione in mercury tolerance resembles its function under cadmium stress in Arabidopsis. *Metallomics* **2014,** *6*, 356.

(30) Raab, A.; Schat, H.; Meharg, A. A.; Feldmann, J., Uptake, translocation and transformation of arsenate and arsenite in sunflower (*Helianthus annuus*): formation of arsenic-phytochelatin complexes during exposure to high arsenic concentrations. *New Phytol.* **2005,** *168*, 551-558.

(31) Bluemlein, K.; Raab, A.; Feldmann, J., Stability of arsenic peptides in plant extracts: off-line versus on-line parallel elemental and molecular mass spectrometric detection for liquid chromatographic separation. *Anal. Bioanal. Chem.* **2009,** *393*, 357-366.

(32) Carey, A. M.; Lombi, E.; Donner, E.; de Jonge, M. D.; Punshon, T.; Jackson, B. P.; Guerinot, M. L.; Price, A. H.; Meharg, A. A., A review of recent developments in the speciation and location of arsenic and selenium in rice grain *Anal. Bioanal. Chem.* **2012,** *401*, 3275-3286.

(33) Raab, A.; Feldmann, J.; Meharg, A. A., The nature of arsenic-phytochelatin complexes in *Holcus lanatus* and *Pteris cretica*. *Plant Physiol.* **2004,** *134*, 1113-1122.

(34) Manceau, A.; Marcus, M. A.; Tamura, N., Quantitative speciation of heavy metals in soils and sediments by synchrotron X-ray techniques. In *Applications of Synchrotron Radiation in Low-Temperature Geochemistry and Environmental Science*, Fenter, P. A.; Rivers, M. L.; Sturchio, N. C.; Sutton, S. R., Eds. Mineralogical Society of America: Washington, DC, 2002; Vol. 49, pp 341-428.

(35) Grafe, M.; Donner, E.; Collins, R. N.; Lombi, E., Speciation of metal(loid)s in environmental samples by X-ray absorption spectroscopy: A critical review. *Anal. Chim. Acta* **2014,** *822*, 1-22.

(36) Rajan, M.; Darrow, J.; Hua, M.; Barnett, B.; Mendoza, M.; Greenfield, B. K.; Andrews, J. C., Hg L_3 XANES study of mercury methylation in shredded *Eichhornia crassipes*. *Environ. Sci. Technol.* **2008,** *42*, 5568-5573.

(37) Patty, C.; Barnett, B.; Mooney, B.; Kahn, A.; Levy, S.; Liu, Y. J.; Pianetta, P.; Andrews, J. C., Using X-ray microscopy and Hg L_3 XANES to study Hg binding in the rhizosphere of *Spartina* cordgrass. *Environ. Sci. Technol.* **2009,** *43*, 7397-7402.

(38) McNear, D. H.; Afton, S. E.; Caruso, J. A., Exploring the structural basis for selenium/mercury antagonism in *Allium fistulosum*. *Metallomics* **2012,** *4*, 267-276.

(39) Zhao, J.; Gao, Y.; Li, Y. F.; Hu, Y. L.; Peng, X. Z.; Dong, Y.; Li, B.; Chen, C.; Chai, Z., Selenium inhibits the phytotoxicity of mercury in garlic (*Allium sativum*). *Environ. Res.* **2013,** *125*, 75–81.

(40) Meng, B.; Feng, X. B.; Qiu, G. L.; Anderson, C. W. N.; Wang, J. X.; Zhao, L., Localization and speciation of mercury in brown rice with implications for pan-Asian public health. *Environ. Sci. Technol.* **2014,** *48*, 7974-7981.

(41) Kodre, A.; Arčon, I.; Debeljak, M.; Potisek, M.; Likar, M.; Vogel-Mikuš, K., Arbuscular mycorrhizal fungi alter Hg root uptake and ligand environment as studied by X-ray absorption fine structure. *Environ. Exp. Bot.* **2017,** *133*, 12-13.

(42) Xu, X. H.; Zhao, J. T.; Li, Y. Y.; Fan, Y. Q.; Zhu, N. L.; Gao, Y. X.; Li, B.; Liu, H. Y.; Li, Y. F., Demethylation of methylmercury in growing rice plants: An evidence of self-detoxification. *Environ. Poll.* **2016,** *210*, 113-120.

(43) Li, P.; Feng, X. B.; Qiu, G. L.; Shang, L. H.; Wang, S. F., Mercury pollution in Wuchuan mercury mining area, Guizhou, Southwestern China: The impacts from large scale and artisanal mercury mining. *Environ. Intern.* **2012,** *42*, 59-66.

(44) Du, X.; Zhu, Y. G.; Liu, W. J.; Zhao, X. S., Uptake of mercury (Hg) by seedlings of rice (*Oryza sativa* L.) grown in solution culture and interactions with arsenate uptake. *Environ. Exp. Bot.* **2005,** *54*, 1-7.

(45) Rovezzi, M.; Lapras, C.; Manceau, A.; Glatzel, P.; Verbeni, R., High energy-resolution x-ray spectroscopy at ultra-high dilution with spherically bent crystal analyzers of 0.5 m radius. *Rev. Sci. Instr.* **2017,** *88*, 013108.

(46) Manceau, A.; Enescu, M.; Simionovici, A.; Lanson, M.; Gonzalez-Rey, M.; Rovezzi, M.; Tucoulou, R.; Glatzel, P.; Nagy, K. L.; Bourdineaud, J.-P., Chemical forms of mercury in human hair reveal sources of exposure. *Environ. Sci. Technol.* **2016,** *50*, 10721–10729.

(47) Manceau, A.; Lemouchi, C.; Enescu, M.; Gaillot, A.-C.; Lanson, M.; Magnin, V.; Glatzel, P.; Poulin, B. A.; Ryan, J. N.; Aiken, G. R.; Gautier-Luneau, I.; Nagy, K. L., Formation of mercury sulfide from Hg(II)-thiolate complexes in natural organic matter. *Environ. Sci. Technol.* **2015,** *49*, 9787−9796.

(48) Lannes, A.; Manceau, A.; Rovezzi, M.; Glatzel, P.; Joly, Y.; Gautier-Luneau, I., Intramolecular Hg...π interactions of d-character with non-bridging atoms in mercury-aryl complexes. *Dalton Trans.* **2016,** *45*, 14035-14038.

(49) Manceau, A.; Marcus, M.; Lenoir, T., Estimating the number of pure chemical components in a mixture by X-ray absorption spectroscopy. *J. Synchrotron Radiat.* **2014,** *21*, 1140-1147.

(50) Wilcox, J.; Rupp, E.; Ying, S. C.; Lim, D. H.; Negreira, A. S.; Kirchofer, A.; Feng, F.; Lee, K., Mercury adsorption and oxidation in coal combustion and gasification processes. *Int. J. Coal Geol.* **2012,** *90*, 4-20.

(51) Lim, D. H.; Wilcox, J., Heterogeneous mercury oxidation on Au(111) from first principles. *Environ. Sci. Technol.* **2013,** *47*, 8515-8522.

(52) Enescu, M.; Manceau, A., High-level ab initio calculation of the stability of mercury–thiolate complexes. *Theor. Chem. Acc.* **2014,** *133*, n° 1457.

(53) Manceau, A.; Lemouchi, C.; Rovezzi, M.; Lanson, M.; Glatzel, P.; Nagy, K. L.; Gautier-Luneau, I.; Joly, Y.; Enescu, M., Structure, bonding, and stability of mercury complexes with thiolate and thioether ligands from high-resolution XANES spectroscopy and first-principles calculations. *Inorg. Chem.* **2015,** *54*, 11776−11791.

(54) Tang, X. Y.; Zheng, A. X.; Shang, H.; Yuan, R. X.; Li, H. X.; Ren, Z. G.; Lang, J. P., Binding of a coordinatively unsaturated mercury(II) thiolate compound by carboxylate anions. *Inorg. Chem.* **2011,** *50*, 503-516.

(55) Møller, C.; Plesset, M. S., Note on an approximation treatment for many-electron systems. *Phys. Rev.* **1934,** *46*, 618-622.

(56) Neese, F., The ORCA program system. *WIREs Comput. Mol. Sci.* **2012,** *2*, 73-78.

(57) Enescu, M.; Nagy, K. L.; Manceau, A., Nucleation of mercury sulfide by dealkylation. *Sci. Rep.* **2016,** *6*, 39359.

(58) Obrist, D.; Pokharel, A. K.; Moore, C., Vertical profile measurements of soil air suggest immobilization of gaseous elemental mercury in mineral soil. *Environ. Sci. Technol.* **2014,** *48*, 2242-2252.

(59) Qiu, G. L.; Feng, X. B.; Wang, S. F.; Shang, L. H., Environmental contamination of mercury from Hg-mining areas in Wuchuan, northeastern Guizhou, China. *Environ. Poll.* **2006,** *142*, 549-558.

(60) Frescholtz, T. F.; Gustin, M. S.; Schorran, D. E.; Fernandez, G. C. J., Assessing the source of mercury in foliar tissue of quaking aspen. *Environ. Toxicol. Chem.* **2003,** *22*, 2114-2119.

(61) Ericksen, J. A.; Gustin, M. S.; Schorran, D. E.; Johnson, D. W.; Lindberg, S. E.; Coleman, J. S., Accumulation of atmospheric mercury in forest foliage. *Atm. Environ.* **2003,** *37*, 1613-1622.

(62) Millhollen, A. G.; Gustin, M. S.; Obrist, D., Foliar mercury accumulation and exchange for three tree species. *Environ. Sci. Technol.* **2006,** *40*, 6001-6006.

(63) Millhollen, A. G.; Obrist, D.; Gustin, M. S., Mercury accumulation in grass and forb species as a function of atmospheric carbon dioxide concentrations and mercury exposures in air and soil. *Chemosphere* **2006,** *65*, 889-897.

(64) Laacouri, A.; Nater, E. A.; Kolka, R. K., Distribution and uptake dynamics of mercury in leaves of common deciduous tree species in Minnesota, USA. *Environ. Sci. Technol.* **2013,** *47*, 10462-10470.

(65) Cavallini, A.; Natali, L.; Durante, M.; Maserti, B., Mercury uptake, distribution and DNA affinity in durum wheat (*Triticum durum* Desf.) plants. *Sci. Tot. Environ.* **1999,** *243*, 119-127.

(66) Cui, L. W.; Feng, X. B.; Lin, C. J.; Wang, X. M.; Meng, B.; Wang, X.; Wang, H., Accumulation and translocation of ^{198}Hg in four crop species. *Environ. Toxicol. Chem.* **2014,** *33*, 334-340.

(67) Jew, A. D.; Kim, C. S.; Rytuba, J. J.; Gustin, M. S.; Brown, G. E., New technique for quantification of elemental Hg in mine wastes and its implications for mercury evasion into the atmosphere. *Environ. Sci. Technol.* **2011,** *45*, 412–417.

(68) Skyllberg, U.; Bloom, P. R.; Qian, J.; Lin, C. M.; Bleam, W. F., Complexation of mercury(II) in soil organic matter: EXAFS evidence for linear two-coordination with reduced sulfur groups. *Environ. Sci. Technol.* **2006,** *40*, 4174-4180.

(69) Nagy, K. L.; Manceau, A.; Gasper, J. D.; Ryan, J. N.; Aiken, G. R., Metallothionein-like multinuclear clusters of mercury(II) and sulfur in peat. *Environ. Sci. Technol.* **2011,** *45*, 7298–7306.

(70) Kim, C. S.; Bloom, N. S.; Rytuba, J. J.; Brown, G. E., Mercury speciation by X-ray absorption fine structure spectroscopy and sequential chemical extractions: A comparison of speciation methods. *Environ. Sci. Technol.* **2003,** *37*, 5102-5108.

(71) Potter, R. W.; Barnes, H. L., Phase relations in the binary Hg-S. *Am. Miner.* **1978,** *63*, 1143–1152.

(72) Cardona, M.; Kremer, R. K.; Lauck, R.; Siegle, G.; Munoz, A.; Romero, A. H., Electronic, vibrational, and thermodynamic properties of metacinnabar β-HgS, HgSe, and HgTe. *Phys. Rev. B* **2009,** *80*, 195204

(73) Bell, A. M. T.; Pattrick, R. A. D.; Vaughan, D. J., Structural evolution of aqueous mercury sulphide precipitates: energy-dispersive X-ray diffraction studies. *Min. Mag.* **2010,** *74*, 85-96.

(74) Baldi, F.; Gallo, M.; Daniele, S.; Battistel, D.; Faleri, C.; Kodre, A.; Arcon, I., An extracellular polymeric substance quickly chelates mercury(II) with N-heterocyclic groups. *Chemosphere* **2017,** *176*, 296-304.

(75) Schiering, N.; Kabsch, W.; Moore, M. J.; Distefano, M. D.; Walsh, C. T.; Pai, E. F., Structure of the detoxification catalyst mercuric ion reductase from *Bacillus* sp. strain RC607. *Nature* **1991,** *352*, 168-172.

(76) Pufahl, R. A.; Singer, C. P.; Peariso, K. L.; Lin, S. J.; Schmidt, P. J.; Fahrni, C. J.; Culotta, V. C.; Penner-Hahn, J. E.; Ohalloran, T. V., Metal ion chaperone function of the soluble Cu(I) receptor Atx1. *Science* **1997,** *278*, 853-856.

(77) Steele, R. A.; Opella, S. J., Structures of the reduced and mercury-bound forms of MerP, the periplasmic protein from the bacterial mercury detoxification system. *Biochemistry* **1997,** *36*, 6885-6895.

(78) Rosenzweig, A. C.; Huffman, D. L.; Hou, M. Y.; Wernimont, A. K.; Pufahl, R. A.; O'Halloran, T. V., Crystal structure of the Atx1 metallochaperone protein at 1.02 angstrom resolution. *Structure* **1999,** *7*, 605-617.

(79) Wernimont, A. K.; Huffman, D. L.; Lamb, A. L.; O'Halloran, T. V.; Rosenzweig, A. C., Structural basis for copper transfer by the metallochaperone for the Menkes/Wilson disease proteins. *Nature Str. Biol.* **2000,** *7*, 766-771.

(80) Wilson, J. R.; Leang, C.; Morby, A. P.; Hobman, J. L.; Brown, N. L., MerF is a mercury transport protein: different structures but a common mechanism for mercuric ion transporters? *FEBS Lett.* **2000,** *472*, 78-82.

(81) Serre, L.; Rossy, E.; Pebay-Peyroula, E.; Cohen-Addad, C.; Coves, J., Crystal structure of the oxidized form of the periplasmic mercury-binding protein MerP from Ralstonia metallidurans CH34. *J. Mol. Biol.* **2004,** *339*, 161-171.

(82) Mah, V.; Jalilehvand, F., Glutathione complex formation with mercury(II) in aqueous solution at physiological pH. *Chem. Res. Toxicol.* **2010,** *23*, 1815-1823.

(83) Luczkowski, M.; Zeider, B. A.; Hinz, A. V. H.; Stachura, M.; Chakraborty, S.; Hemmingsen, L.; Huffman, D. L.; Pecoraro, V. L., Probing the coordination environment of the human copper chaperone HAH1: Characterization of Hg^{II}-bridged homodimeric species in solution. *Chem. - Eur. J.* **2013,** *19*, 9042-9049.

(84) Lian, P.; Guo, H. B.; Riccardi, D.; Dong, A. P.; Parks, J. M.; Xu, Q.; Pai, E. F.; Miller, S. M.; Wei, D. Q.; Smith, J. C.; Guo, H., X-ray structure of a Hg^{2+} complex of mercuric reductase (MerA) and quantum mechanical/molecular mechanical study of Hg^{2+} transfer between the C-terminal and buried catalytic site cysteine pairs. *Biochemistry* **2014,** *53*, 7211-7222.

(85) Muradoglu, F.; Gündogdu, M., Stomata size and frequency in some walnut (*Juglans regia*) cultivars. *Int. J. Agric. Biol.* **2011,** *13*, 1011–1015.

(86) Bondada, B.; Tu, C.; Ma, L., Surface structure and anatomical aspects of Chinese brake fern (*Pteris vittata*; Pteridaceae). *Brittonia* **2006,** *58*, 217-228.

(87) Lee, J.; Shim, D.; Song, W. Y.; Hwang, I.; Lee, Y., Arabidopsis metallothioneins 2a and 3 enhance resistance to cadmium when expressed in *Vicia faba* guard cells. *Plant Mol. Biol.* **2004,** *54*, 805-815.

(88) Peroza, E. A.; Schmucki, R.; Guntert, P.; Freisinger, E.; Zerbe, O., The β_E-domain of wheat E_c-1 metallothionein: A metal-binding domain with a distinctive structure. *J. Mol. Biol.* **2009,** *387*, 207-218.

(89) Freisinger, E., The metal-thiolate clusters of plant metallothioneins. *Chimia* **2010,** *64*, 217-224.

(90) Perfus-Barbeoch, L.; Leonhardt, N.; Vavasseur, A.; Forestier, C., Heavy metal toxicity: cadmium permeates through calcium channels and disturbs the plant water status. *Plant J.* **2002,** *32*, 539-548.

(91) Zhu, M.; Zhu, N. L.; Song, W. Y.; Harmon, A. C.; Assmann, S. M.; Chen, S., Thiol-based redox proteins in *Brassica napus* guard cell abscisic acid and methyl jasmonate signaling. *Plant J.* **2014,** *78*, 491-515.

(92) Peroza, E. A.; Al Kaabi, A.; Meyer-Klaucke, W.; Wellenreuther, G.; Freisinger, E., The two distinctive metal ion binding domains of the wheat metallothionein E_c-1. *J. Inorg. Biochem.* **2009,** *103*, 342-353.

(93) Loebus, J.; Peroza, E. A.; Bluthgen, N.; Fox, T.; Meyer-Klaucke, W.; Zerbe, O.; Freisinger, E., Protein and metal cluster structure of the wheat metallothionein domain γ-E-c-1: the second part of the puzzle. *J. Biol. Inorg. Chem.* **2011,** *16*, 683-694.

(94) Tarasava, K.; Freisinger, E., Investigating the influence of histidine residues on the metal ion binding ability of the wheat metallothionein γ-E_c-1 domain. *J. Inorg. Biochem.* **2015,** *153*, 197-203.

(95) Freisinger, E., Spectroscopic characterization of a fruit-specific metallothionein: *M. acuminata* MT3. *Inorg. Chim. Acta* **2007,** *360*, 369-380.

(96) Domenech, J.; Mir, G.; Huguet, G.; Capdevila, M.; Molinas, M.; Atrian, S., Plant metallothionein domains: functional insight into physiological metal binding and protein folding. *Biochimie* **2006,** *88*, 583-593.

(97) Romero-Isart, N.; Vasak, M., Advances in the structure and chemistry of metallothioneins. *J. Inorg. Biochem* **2002,** *88*, 388-396.

(98) Freisinger, E., Plant MTs-long neglected members of the metallothionein superfamily. *Dalton Trans.* **2008,** *47*, 6663-6675.

(99) Freisinger, E., Structural features specific to plant metallothioneins. *J. Biol. Inorg. Chem.* **2011,** *16*, 1035-1045.

(100) Blindauer, C. A.; Harrison, M. D.; Parkinson, J. A.; Robinson, A. K.; Cavet, J. S.; Robinson, N. J.; Sadler, P. J., A metallothionein containing a zinc finger within a four-metal cluster protects a bacterium from zinc toxicity. *Proc. Natl. Acad. Sci. U.S.A.* **2001,** *98*, 9593-9598.

(101) Digilio, G.; Bracco, C.; Vergani, L.; Botta, M.; Osella, D.; Viarengo, A., The cadmium binding domains in the metallothionein isoform Cd-7-MT10 from *Mytilus galloprovincialis* revealed by NMR spectroscopy. *J. Biol. Inorg. Chem.* **2009,** *14*, 167-178.

(102) Schicht, O.; Freisinger, E., Spectroscopic characterization of *Cicer arietinum* metallothionein 1. *Inorg. Chim. Acta* **2009,** *362*, 714.

(103) Bowmaker, G. A.; Dance, I. G.; Harris, R. K.; Henderson, W.; Laban, I.; Scudder, M. L.; Oh, S. W., Crystallographic, vibrational and nuclear magnetic resonance spectroscopic characterization of the $[(PhS)_2Hg(\mu\text{-}SPh)_2Hg(SPh)_2]^{2-}$ ion. *J. Chem. Soc.-Dalton Trans.* **1996**, 2381-2388.

(104) Melnick, J. G.; Yurkerwich, K.; Parkin, G., On the chalcogenophilicity of mercury: Evidence for a strong Hg-Se bond in $[Tm^{But}]HgSePh$ and its relevance to the toxicity of mercury. *J. Am. Chem. Soc.* **2010,** *132*, 647-655.

(105) Bowmaker, G. A.; Dance, I. G.; Dobson, B. C.; Rogers, D. A., Syntheses and vibrational spectra of some tris(alkanethiolato)mercurate(II) complexes, and crystal structure of the Hexakis(methanethiolato)dimercurate(II) dianion. *Aust. J. Chem.* **1984,** *37*, 1607-1618.

(106) Enescu, M.; Renault, J. P.; Pommeret, S.; Mialocq, J. C.; Pin, S., *Ab initio* study of Cd–thiol complexes: application to the modelling of the metallothionein active site. *Phys. Chem. Chem. Phys.* **2003,** *5*, 3762–3767.

(107) Manceau, A.; Nagy, K. L., Relationships between Hg(II)-S bond distance and Hg(II) coordination in thiolates. *Dalton Trans.* **2008,** *11*, 1421-1425.

(108) Rodic, D.; Spasojevic, V.; Bajorek, A.; Onnerud, P., Similarity of structure properties of $Hg_{1-x}Mn_xS$ and $Cd_{1-x}Mn_xS$ (structure properties of HgMnS and CdMnS). *J. Mag. Mag. Mater.* **1996,** *152*, 159-164.

(109) Frenkel, A. I.; Yevick, A.; Cooper, C.; Vasic, R., Modeling the structure and composition of nanoparticles by extended X-ray absorption fine-structure spectroscopy. In *Ann. Rev. Anal. Chem.*, Cooks, R. G.; Yeung, E. S., Eds. 2011; Vol. 4, pp 23-39.

(110) Ankudinov, A. L.; Rehr, J. J.; Low, J. J.; Bare, S. R., Sensitivity of Pt x-ray absorption near edge structure to the morphology of small Pt clusters. *J. Chem. Phys.* **2002,** *116*, 1911-1919.

(111) Demchenko, I. N.; Denlinger, J. D.; Chernyshova, M.; Yu, K. M.; Speaks, D. T.; Olalde-Velasco, P.; Hemmers, O.; Walukiewicz, W.; Derkachova, A.; Lawniczak-Jablonska, K., Full multiple scattering analysis of XANES at the Cd L_3 and O *K* edges in CdO films combined with a soft-x-ray emission investigation. *Phys. Rev. B* **2010,** *82*, 075107.

(112) Gardea-Torresdey, J. L.; Tiemann, K. J.; Parsons, J. G.; Gamez, G.; Herrera, I.; Jose-Yacaman, M., XAS investigations into the mechanism(s) of Au(III) binding and reduction by alfalfa biomass. *Microchem. J.* **2002,** *71*, 193-204.

(113) Gardea-Torresdey, J. L.; Parsons, J. G.; Gomez, E.; Peralta-Videa, J.; Troiani, H. E.; Santiago, P.; Yacaman, M. J., Formation and growth of Au nanoparticles inside live alfalfa plants. *Nano Lett.* **2002,** *4*, 397-401.

(114) Gardea-Torresdey, J. L.; Gomez, E.; Peralta-Videa, J. R.; Parsons, J. G.; Troiani, H. E.; Yacaman, M. J., Alfalfa sprouts: A natural source for the synthesis of silver nanoparticles. *Langmuir* **2003,** *19*, 1357-1361.

(115) Manceau, A.; Nagy, K. L.; Marcus, M. A.; Lanson, M.; Geoffroy, N.; Jacquet, T.; Kirpichtchikova, T., Formation of metallic copper nanoparticles at the soil-root interface. *Environ. Sci. Technol.* **2008,** *42*, 1766-1772.

(116) Das, R. K.; Pachapur, V. L.; Linson Lonappan, L.; Naghdi, M.; Pulicharla, R.; Maiti, S.; Cledon, M.; Dalila, L. M. A.; Sarma, S. J.; Brar, S. K., Biological synthesis of metallic nanoparticles: plants, animals and microbial aspects. *Nanotechnol. Environ. Eng.* **2017,** *2*, 18.

(117) Marcos, E.; Basanta, B.; Chidyausiku, T. M.; Tang, Y.; Oberdorfer, G.; Liu, G.; Swapna, G. V. T.; Guan, R.; Silva, D. A.; Jiayi Dou; Pereira, J. H.; Xiao, R.; Sankaran, B.; Zwart, P. H.; Montelione, G. T.; Baker, D., Principles for designing proteins with cavities formed by curved β sheets. *Science* **2017,** *355*, 201-206.

(118) Frazier, J. M.; George, S. S.; Overnell, J.; Coombs, T. L.; Kagi, J., Characterization of two molecular weight classes of cadmium binding proteins from the mussel, *Mytilus edulis* (L). *Comp. Biochem. Physiol. C* **1985,** *80*, 257-262.

(119) Frazier, J. M., Cadmium-binding proteins in the Mussel, *Mytilus edulis*. *Environ. Health Persp.* **1986,** *65*, 39-43.

(120) Mackay, E. A.; Overnell, J.; Dunbar, B.; Davidson, I.; Hunziker, P. E.; Kagi, J. H. R.; Fothergill, J. E., Complete amino acid sequences of five dimeric and four monomeric forms of metallothionein from the edible mussel *Mytilus edulis*. *Eur. J. Biochem.* **1993,** *218*, 183-194.

(121) Barsyte, D.; White, K. N.; Lovejoy, D. A., Cloning and characterization of metallothionein cDNAs in the mussel *Mytilus edulis* L. digestive gland. *Comp. Biochem. Physiol. C* **1999,** *122*, 287-296.

(122) Lemoine, S.; Bigot, Y.; Sellos, D.; Cosson, R. P.; Laulier, M., Metallothionein isoforms in *Mytilus edulis* (Mollusca, Bivalvia): Complementary DNA characterization and quantification of expression in different organs after exposure to cadmium, zinc, and copper. *Marine Biotechnol.* **2000,** *2*, 195-203.

(123) Ivankovic, D.; Pavicic, J.; Kozar, S.; Raspor, B., Multiple forms of metallothionein from the digestive gland of naturally occurring and cadmium-exposed mussels, *Mytilus galloprovincialis*. *Helgol. Mar. Res.* **2002,** *56*, 95-101.

(124) Kim, J. S.; Rees, D. C., Structural models for the metal centers in the nitrogenase molybdenum-iron protein. *Science* **1992,** *257*, 1677-1682.

(125) Lee, G. S. H.; Fisher, K. J.; Vassallo, A. M.; Hanna, J. V.; Dance, I. G., Solid-state ^{113}Cd NMR of three structural isomers of $[S_4Cd_{10}(SPh]_{16}]^{4-}$. *Inorg. Chem.* **1993,** *32*, 66-72.

(126) Beinert, H.; Holm, R. H.; Munck, E., Iron-sulfur clusters: Nature's modular, multipurpose structures. *Science* **1997,** *277*, 653-659.

(127) Gelinsky, M.; Vahrenkamp, H., Oligonuclear benzylthiolate zinc complexes. *Z. Anorg. Allg. Chem.* **2002,** *628*, 1017-1021.

(128) Rao, P. V.; Holm, R. H., Synthetic analogues of the active sites of iron-sulfur proteins. *Chem. Rev.* **2004,** *104*, 527-559.

(129) Fritsch, J.; Scheerer, P.; Frielingsdorf, S.; Kroschinsky, S.; Friedrich, B.; Lenz, O.; Spahn, C. M. T., The crystal structure of an oxygen-tolerant hydrogenase uncovers a novel iron-sulphur centre. *Nature* **2011**, 249-U134.

(130) Pan, Y. H.; Sader, K.; Powell, J. J.; Bleloch, A.; Gass, M.; Trinick, J.; Warley, A.; Li, A.; Brydson, R.; Brown, A., 3D morphology of the human hepatic ferritin mineral core: New evidence for a subunit structure revealed by single particle analysis of HAADF-STEM images. *J. Str. Biol.* **2009,** *166*, 22-31.

(131) Jian, N.; Dowle, M.; Horniblow, R. D.; Tselepis, C.; Palmer, R. E., Morphology of the ferritin iron core by aberration corrected scanning transmission electron microscopy. *Nanotechnol.* **2016,** *27*, 46LT02.

(132) Pozzi, C.; Ciambellotti, S.; Bernacchioni, C.; Di Pisa, F.; Mangani, S.; Turano, P., Chemistry at the protein-mineral interface in L-ferritin assists the assembly of a functional (μ^3-oxo)Tris (μ^2-peroxo) triiron(III) cluster. *Proc. Natl. Acad. Sci. U.S.A.* **2017,** *114*, 2580-2585.

(133) Pires, S.; Habjanic, J.; Sezer, M.; Soares, C. M.; Hemmingsen, L.; Iranzo, O., Design of a peptidic turn with high affinity for Hg^{II}. *Inorg. Chem.* **2012,** *51*, 11339-11348.

(134) Brust, M.; Walker, M.; Bethell, D.; Schiffrin, D. J.; Whyman, R., Synthesis of thiol-derivatised gold nanoparticles in a two-phase liquid-liquid system. *J. Chem. Soc., Chem. Commun.* **1994,** *7*, 801-802.

(135) Higginson, K. A.; Kuno, M.; Bonevich, J.; Qadri, S. B.; Yousuf, M.; Mattoussi, H., Synthesis and characterization of colloidal β-HgS quantum dots. *J. Phys. Chem. B* **2002,** *106*, 9982-9985.

(136) Zhang, P.; Sham, T. K., X-ray studies of the structure and electronic behavior of alkanethiolate-capped gold nanoparticles: The interplay of size and surface effects. *Phys. Rev. Lett.* **2003,** *90*, 245502.

(137) Frenkel, A. I.; Nemzer, S.; Pister, I.; Soussan, L.; Harris, T.; Sun, Y.; Rafailovich, M. H., Size-controlled synthesis and characterization of thiol-stabilized gold nanoparticles. *J. Chem. Phys.* **2005,** *123*, 208-213.

(138) Jadzinsky, P. D.; Calero, G.; Ackerson, C. J.; Bushnell, D. A.; Kornberg, R. D., Structure of a thiol monolayer-protected gold nanoparticle at 1.1 angstrom resolution. *Science* **2007,** *318*, 430-433.

(139) Whetten, R. L.; Price, R. C., Nano-golden order. *Science* **2007,** *318*, 407-408.

(140) Simms, G. A.; Padmos, J. D.; Zhang, P., Structural and electronic properties of protein/thiolate-protected gold nanocluster with "staple" motif: A XAS, L-DOS, and XPS study. *J. Chem. Phys.* **2009,** *131*, 214703.

(141) Ariyasu, S.; Onoda, A.; Sakamoto, R.; Yamamura, T., Conjugation of Au11 cluster with Cys-rich peptides containing the α-domain of metallothionein. *Dalton Trans.* **2009,** *19*, 3742-3747.

(142) Liu, X.; Liu, R.; Tang, Y. R.; Zhang, L. C.; Hou, X. D.; Lv, Y., Antibody-biotemplated HgS nanoparticles: Extremely sensitive labels for atomic fluorescence spectrometric immunoassay. *Analyst* **2012,** *137*, 1473-1480.

(143) Schwerdtfeger, P.; Li, J.; Pyykko, P., The polarizability of Hg and the ground-state interaction potential of Hg_2. *Theor. Chim. Acta* **1994,** *87*, 313-320.

(144) Pyykko, P.; Straka, M., Ab initio studies of the dimers $(HgH_2)_2$ and $(HgMe_2)_2$. Metallophilic attraction and the van der Waals radii of mercury. *Phys. Chem. Chem. Phys.* **2000,** *2*, 2489-2493.

(145) Capdevila, M.; Domenech, J.; Pagani, A.; Tio, L.; Villarreal, L.; Atrian, S., Zn- and Cd-metallothionein recombinant species from the most diverse phyla may contain sulfide (S^{2-}) ligands. *Angew. Chem., Int. Ed.* **2005,** *44*, 4618-4622.

(146) Alvarez, C.; Calo, L.; Romero, L. C.; Garcia, I.; Gotor, C., An O-acetylserine(thiol)lyase homolog with L-cysteine desulfhydrase activity regulates cysteine homeostasis in Arabidopsis. *Plant Phys.* **2010,** *152*, 656-669.

(147) Thomas, S. A.; Gaillard, J. F., Cysteine addition promotes sulfide production and four-fold Hg(II)-S coordination in actively metabolizing *Escherichia coli*. *Environ. Sci. Technol.* **2017,** *51*, 4642-4651.

(148) Jia, H. L.; Wang, X. F.; Dou, Y. H.; Liu, D.; Si, W. T.; Fang, H.; Zhao, C.; Chen, S. L.; Xi, J. J.; Li, J. S., Hydrogen sulfide - cysteine cycle system enhances cadmium tolerance through alleviating cadmium-induced oxidative stress and ion toxicity in Arabidopsis roots. *Sci. Rep.* **2016,** *6*, 39702.

(149) Ye, H.; Garifullina, G. F.; Abdel-Ghany, S. E.; Zhang, L. H.; Pilon-Smits, E. A. H.; Pilon, M., The chloroplast NifS-like protein of *Arabidopsis thaliana* is required for iron-sulfur cluster formation in ferredoxin. *Planta* **2005,** *220*, 602-608.

(150) Li, Q.; Cao, J. H., Structure of leaf epidermis and ecology adaptation of *Vitex negundo* L. at Karat area in southwest China. *J. Henan Normal Univ.* **2008,** *36*, 131-134.

(151) Driscoll, S. P.; Prins, A.; Olmos, E.; Kunert, K. J.; Foyer, C. H., Specification of adaxial and abaxial stomata, epidermal structure and photosynthesis to CO_2 enrichment in maize leaves. *J. Exp. Bot.* **2006,** *57*, 381-390.

(152) Waldron, K. J.; Rutherford, J. C.; Ford, D.; Robinson, N. J., Metalloproteins and metal sensing. *Nature* **2009,** *460*, 823-830.

(153) Ralston, D. M.; Ohalloran, T. V., Ultrasensitivity and heavy-metal selectivity of the allosterically modulated MerR transcription complex. *Proc. Natl. Acad. Sci. USA* **1990,** *87*, 3846-3850.

(154) Hintelmann, H.; Harris, R.; Heyes, A.; Hurley, J. P.; Kelly, C. A.; Krabbenhoft, D. P.; Lindberg, S.; Rudd, J. W. M.; Scott, K. J.; St Louis, V. L., Reactivity and mobility of new and old mercury deposition in a Boreal forest ecosystem during the first year of the METAALICUS study. *Environ. Sci. Technol.* **2002,** *36*, 5034-5040.

(155) Auvray, P.; Genet, F., Affinement de la structure cristalline du cinabre α-HgS. *Bull. Soc. Fr. Mineral. Cristallogr.* **1973,** *96*, 218–219.

FIGURE LEGENDS

Figure 1. Concentration of mercury in leaf tissues and ambient air (a) and ternary plot of the proportions of the three Hg species in leaf tissues (b). Pv : *Pteris vittata*; Vn: *Vitex negundo*; Ds: *Desmodium sequax wall*; Do: *Debregeasia orientalis*; Jr: *Juglans regia;* Po: *Platycladus orientalis*. The number after each sample code is the concentration in ng Hg mg^{-1} (ppm) dry weight (dwt). Sp1 and Sp2 are two dithiolate complexes. Nano β-HgS is nanoparticulate metacinnabar.[47]

Figure 2. Mercury speciation in the mined Hg ore and in Soil16 by L_3-edge HR-XANES spectroscopy. a) Hg in the ore is in the form of cinnabar (α-HgS). b) At least 90% of the Hg present in Soil16 is precipitated as nanoparticulate metacinnabar (β-HgS_{NP}). The β-HgS_{NP} reference is from the A horizon of a contaminated soil situated downstream from Oak Ridge, TN, in the United States.[47] Polyhedral representations are of the α-HgS and β-HgS structures.[108, 155] Dark red and yellow represent Hg and S, respectively. The α allotrope features an array of parallel …S-Hg-S-

926 Hg-S… chains and the β allotrope a 3D assemblage of corner-sharing HgS_4 tetrahedra. The linear
927 and tetrahedral coordinations of Hg provide distinct spectral signatures.
928
929 **Figure 3.** Mercury speciation in soils by L_3-edge HR-XANES spectroscopy. a) Two dominant Hg
930 forms are present in Soil44 and Soil88: α-HgS represented by the Hg ore spectrum and β-HgS_{NP}
931 represented by the Soil16 spectrum (Figure 2b). b-f) Linear least-squares combination fits of the
932 multicomponent soil spectra with two (2cp) or three (3cp) spectra from single species.
933
934 **Figure 4.** The three outliers spectra from the twenty-four leaf spectra. a) The Ds4 and Pv25 spectra
935 are from single species denoted Sp1 and Sp2, respectively. Their intense near-edge peak is
936 diagnostic of a linear RS-Hg-SR bonding.[53] The near-edge and the following peak (arrow) from
937 Vn6 have lower amplitude and the signal immediately after the edge maximum is shifted left. These
938 changes indicate a tetrahedral coordination with four sulfur atoms as in β-HgS.[53] b) The Ds4
939 spectrum is close to Hg-PC2. c) Linear least-squares fit to the Vn6 spectrum with 45 ± 8 mol %
940 Sp1 and 55 ± 8 mol % β-HgS_{NP}. d) Geometry-optimized Hg-PC2 complex. Hg is bonded to the
941 two cysteinyl S atoms[28] and to two carbonyl oxygens forming a double six-membered *bis*-
942 (oxo)thiolate ring chelate ($Hg(SR+O)_2$ coordination). The peptide forms a scaffold for the Hg
943 complex, and the molecular cage is stabilized by one hydrogen bond between a carbonyl oxygen
944 and an amide proton, as is customary for the secondary structure of proteins. Cartesian coordinates
945 are given in the SI. Dark red, Hg; yellow, S; blue, N; red, O; gray, C; light gray, H.
946
947 **Figure 5.** Estimation of the Hg_xS_y cluster size in plant leaves from the shape of the HR-XANES
948 edge maximum. The upper part of the edge for Po2 and Vn6, which contain 57% and 55% β-HgS_{NP},
949 respectively, is structured (see also Figure 4a) whereas MT2 has a featureless bell-shape. Variations
950 of the absorption signal in this energy region come from medium-range Hg shells, which the MT
951 clusters lack owing to their small size (maximum Hg-Hg distance is ~7 Å).

952

953 **Figure 6.** Detection of a cinnabar (α-HgS) sand-sized grain in a 5 mm diameter pressed pellet from
954 the lyophilized Vn30 leaf tissue. a) 108 HR-XANES spectra were measured for 20 s by rastering a
955 700 x 80 μm^2 (H x V) X-ray beam on the sample pellet. The clump of point spectra is from the leaf
956 tissue. The point spectrum on top with a higher absorbance is from both the leaf tissue and a Hg-
957 rich dust particle which remained at the surface of a leaf during the sample preparation and is now
958 inside the pellet. The group of leaf spectra with a lower absorbance was taken on the pellet rim. b)
959 Comparison of the point spectrum to the average spectrum from the leaf tissue (Vn30) and the Hg
960 ore (well-crystallized α-HgS). c) Linear combination fit.
961

962 **Figure 7.** Polyhedral representation of organic and inorganic Hg_xS_y cluster models. a) Geometry-
963 optimized $Hg_3(SMe)_9$ cluster featuring the binding of Hg to the $Me^{II}_3Cys_9$ site of the MT β_E domain
964 of plants.[88] b) $\{Hg_3S_9\}$ motif of β-HgS showing the analogy of the connectivity of the $\{HgS_4\}$
965 tetrahedra in the organic (MT) and inorganic (β-HgS) Hg_3S_9 clusters. c) Geometry-optimized
966 $Hg_4(SMe)_{11}$ cluster featuring the binding of Hg to the $Me^{II}_4Cys_{11}$ site of the α domain of animal
967 MTs.[97] d) $\{Hg_4S_{10}\}$ motif of β-HgS. The topology is different from that of the $Me^{II}_4Cys_{11}$-α cluster.
968 In a tetranuclear β-HgS-type cluster each tetrahedron shares three bridging sulfurs (μ_2-S type)
969 yielding an adamantane-type cage. In $Me^{II}_4Cys_{11}$-α, only two tetrahedra have three μ_2 bridging
970 sulfurs, and the two other have two μ_2 bridging sulfurs. e) Geometry-optimized $Hg_4(SMe)_{12}$ cluster
971 featuring the binding of Hg to the $Me^{II}_4Cys_{12}$-α site of Mytilidae (MT2 reference). f) $\{Hg_4S_{12}\}$
972 motif of β-HgS. g) Geometry-optimized $Hg_4(SMe)_{10}His$ cluster featuring the binding of Hg to the
973 proposed $Me^{II}_4Cys_{10}His$ site of *Musa acuminata* (banana) MT.[95] The His for Cys substitution
974 marginally modifies the mercury-sulfur coordination. h) Geometry-optimized $Zn_5(SMe)_{12}$ cluster
975 featuring the binding of Hg to the proposed $Me^{II}_5Cys_{12}$ cluster of *Cicer arietinum* (chickpea) MT.[102]
976 The $\{ZnS_4\}$ tetrahedron in the center links two edge-sharing $Zn_2(SMe)_{12}$ complexes. The heavily
977 strained $Hg_5(SMe)_{12}$ cluster is unstable. Cartesian coordinates are given in the SI.

Figure 8. a) L_3-edge HR-XANES spectra of Hg_xS_y clusters in plant leaf (Vn30) and in natural organic matter (Hg-NOM spectrum from ref.[47]). The NOM was reacted with 200 ng Hg(II) mg^{-1} NOM dwt at pH 6 in air-equilibrated water in the dark for 10 days. It contains 3-5 nanometer-sized β-HgS crystals imaged by HRTEM (insert).[47] The modulations in the top-edge region (arrows) are diagnostic of medium-range distance Hg-Hg pairs. In their absence, the absorption signal has a bell-shape (Figure 5).[53] b) Polyhedral representation of a $Hg_7(SMe)_{16}$ cluster with a β-HgS-type local structure. The $\{Hg_7S_{16}\}$[34, 35] motif is from the β-HgS structure,[108] only the positions of the methyl groups (Me) were optimized. Cartesian coordinates are given in the SI.

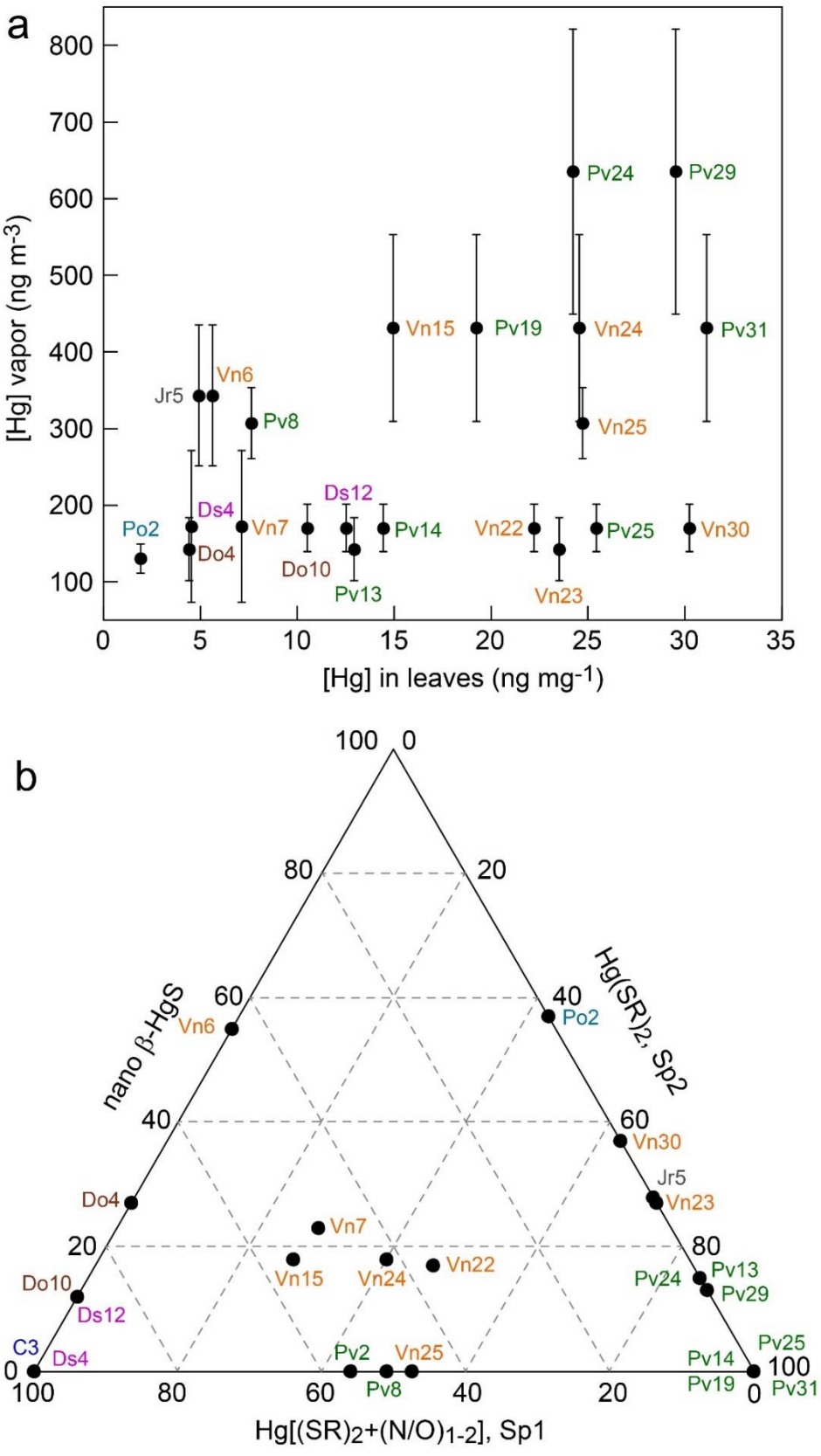

989

990

991 **Figure 1**

992 **Please, print to fit the width of one column, thank you**

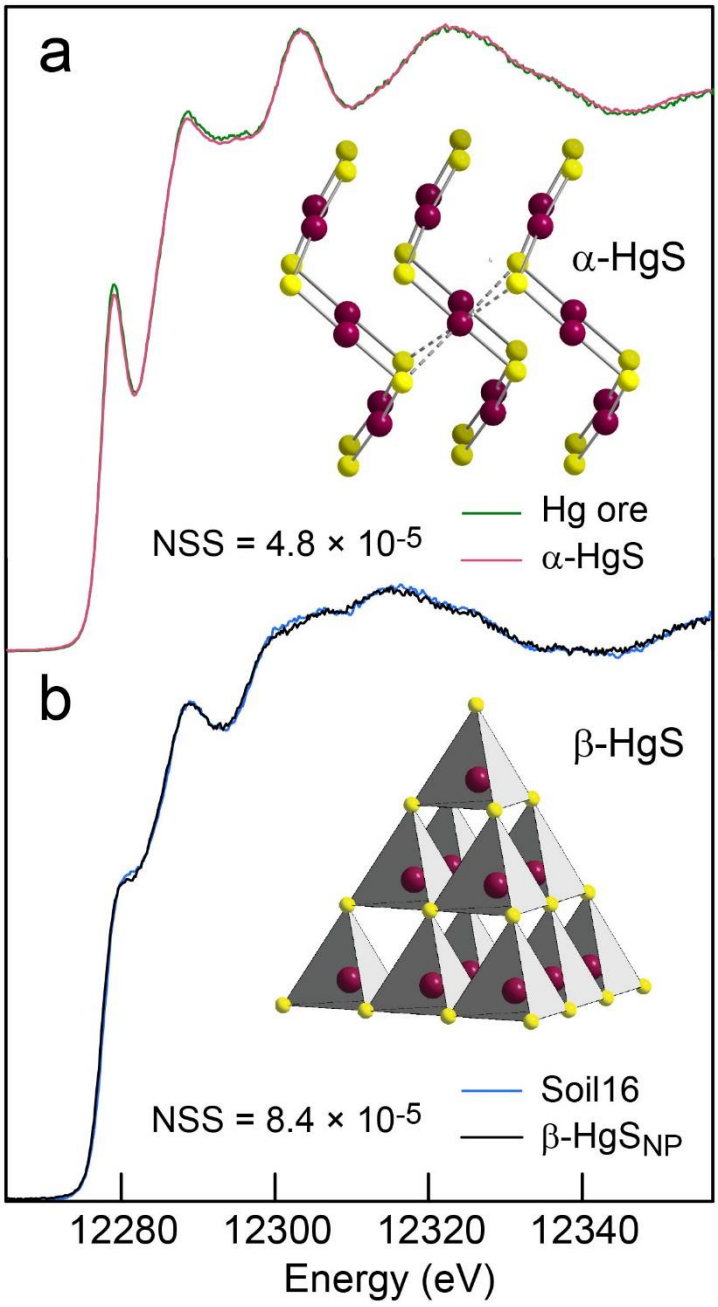

993

994

995 **Figure 2**

996 **Please, print to fit the width of one column, thank you**

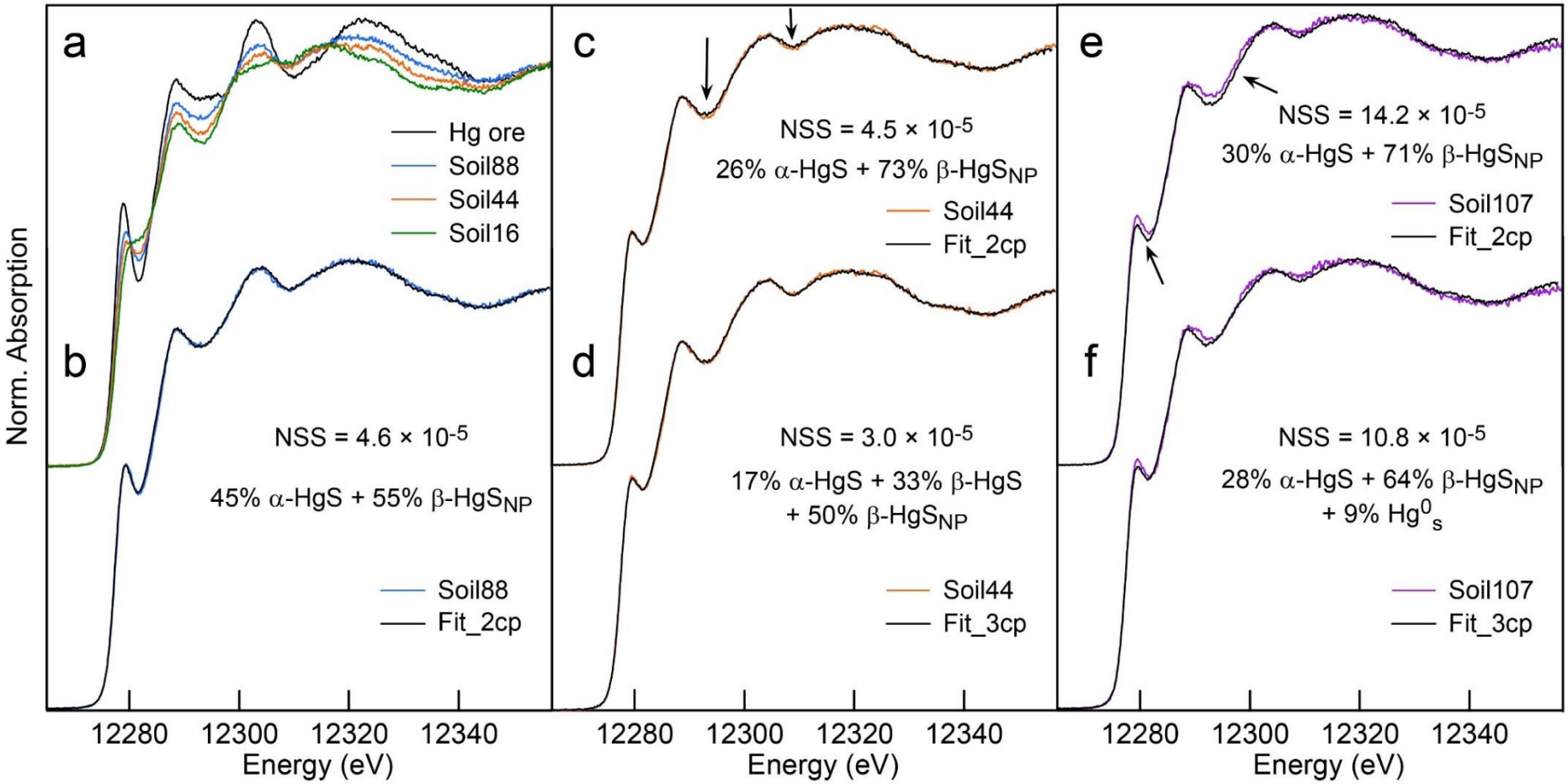

Figure 3

Please, print to fit the width of two columns, thank you

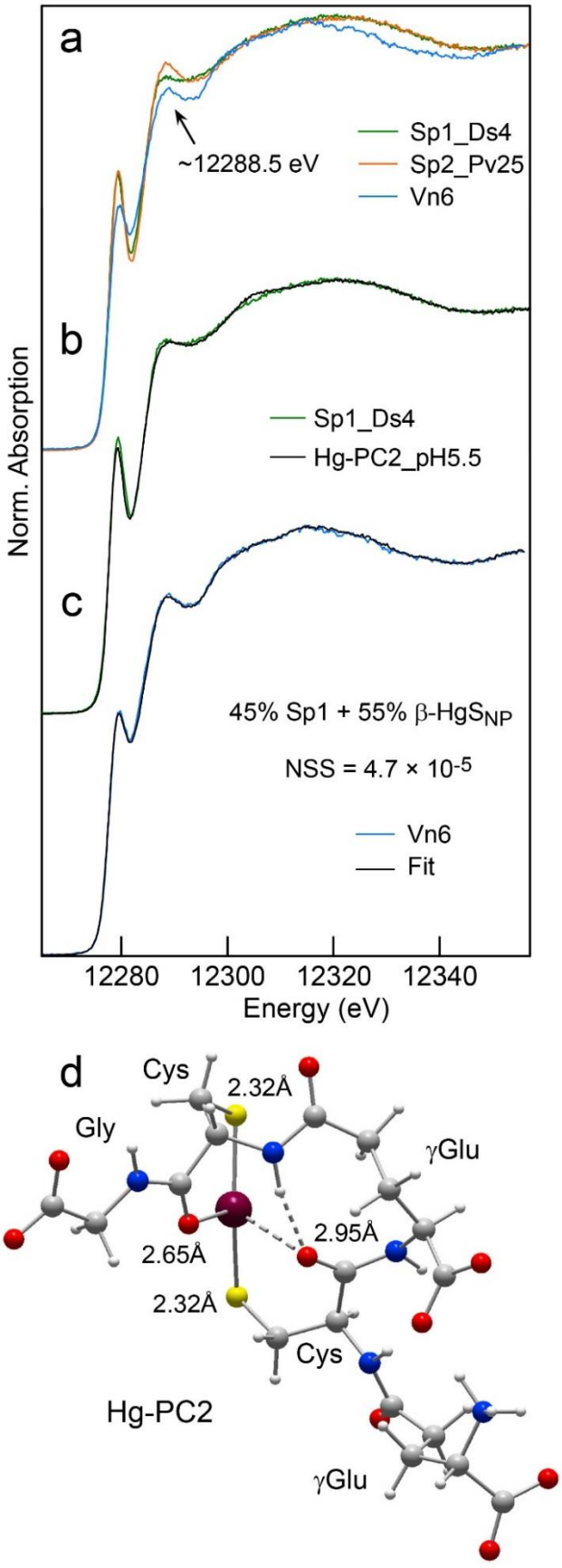

Figure 4

Please, print to fit the width of one column, thank you

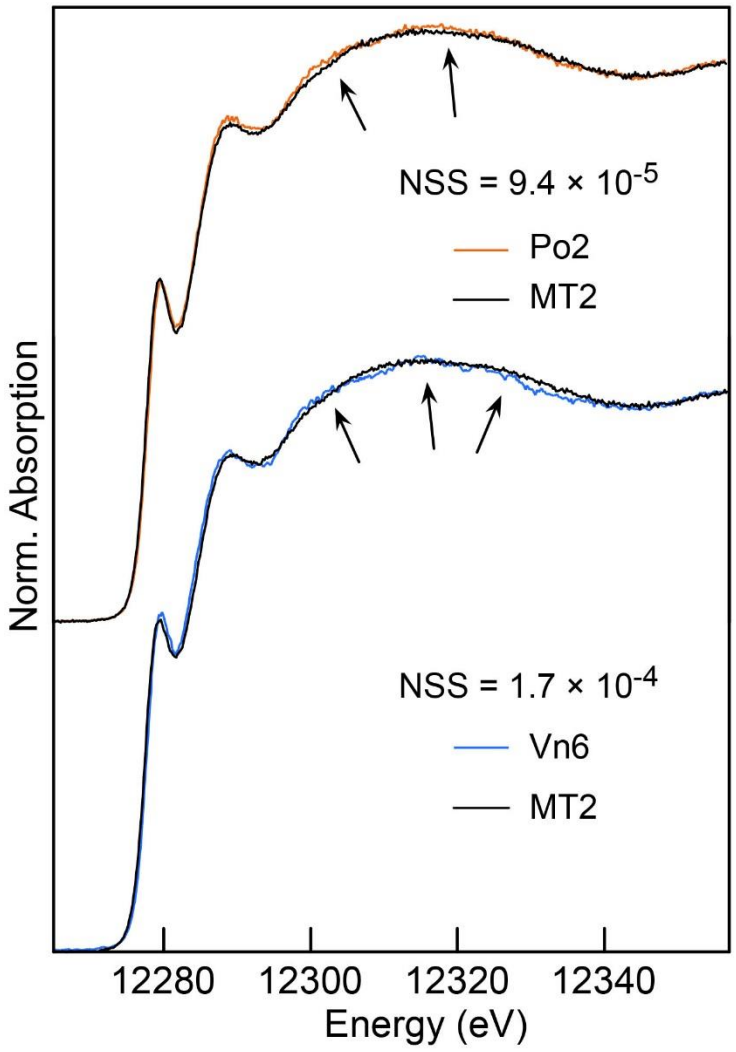

Figure 5

Please, print to fit the width of one column, thank you

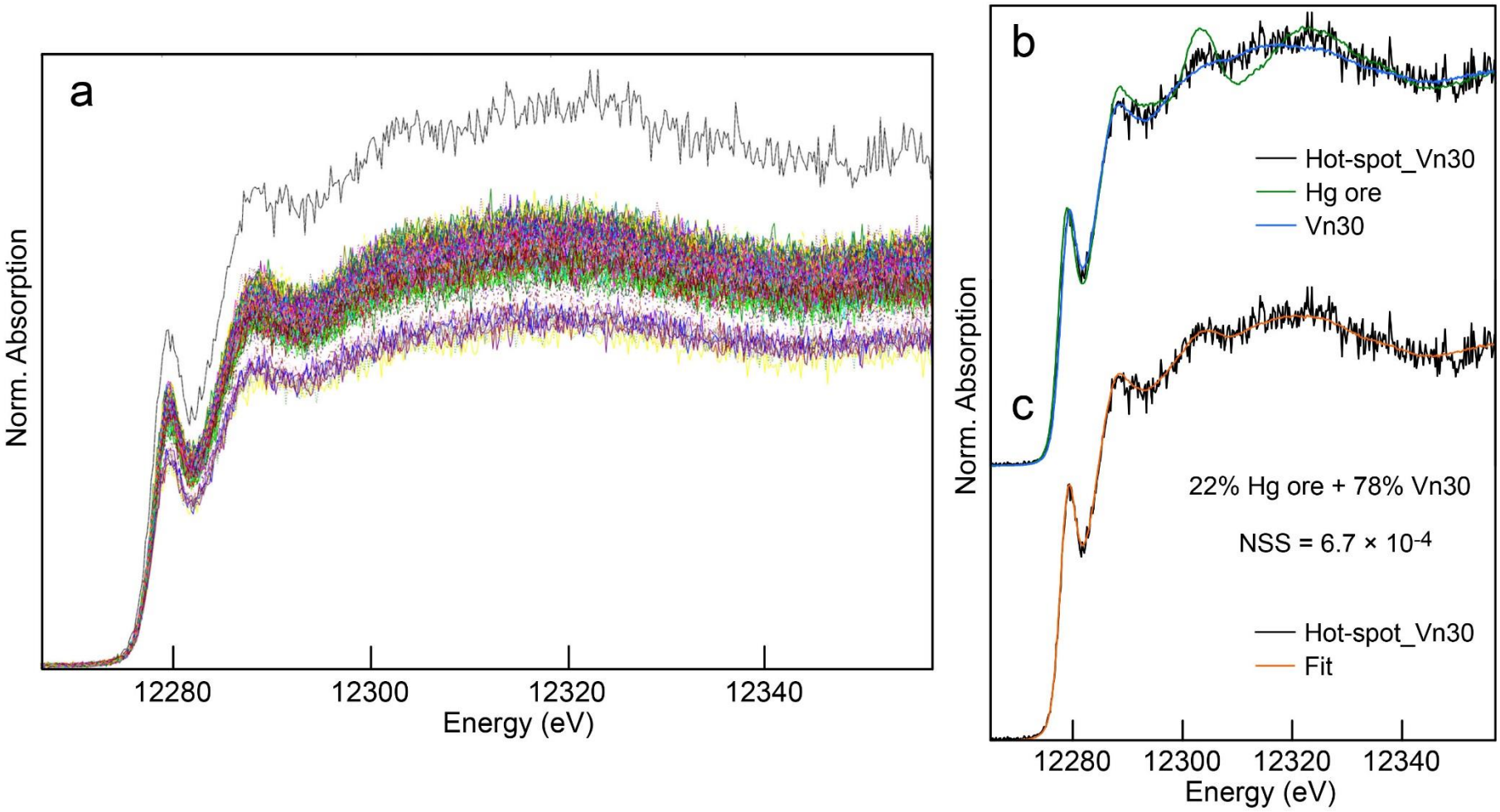

Figure 6

Please, print to fit the width of two columns, thank you

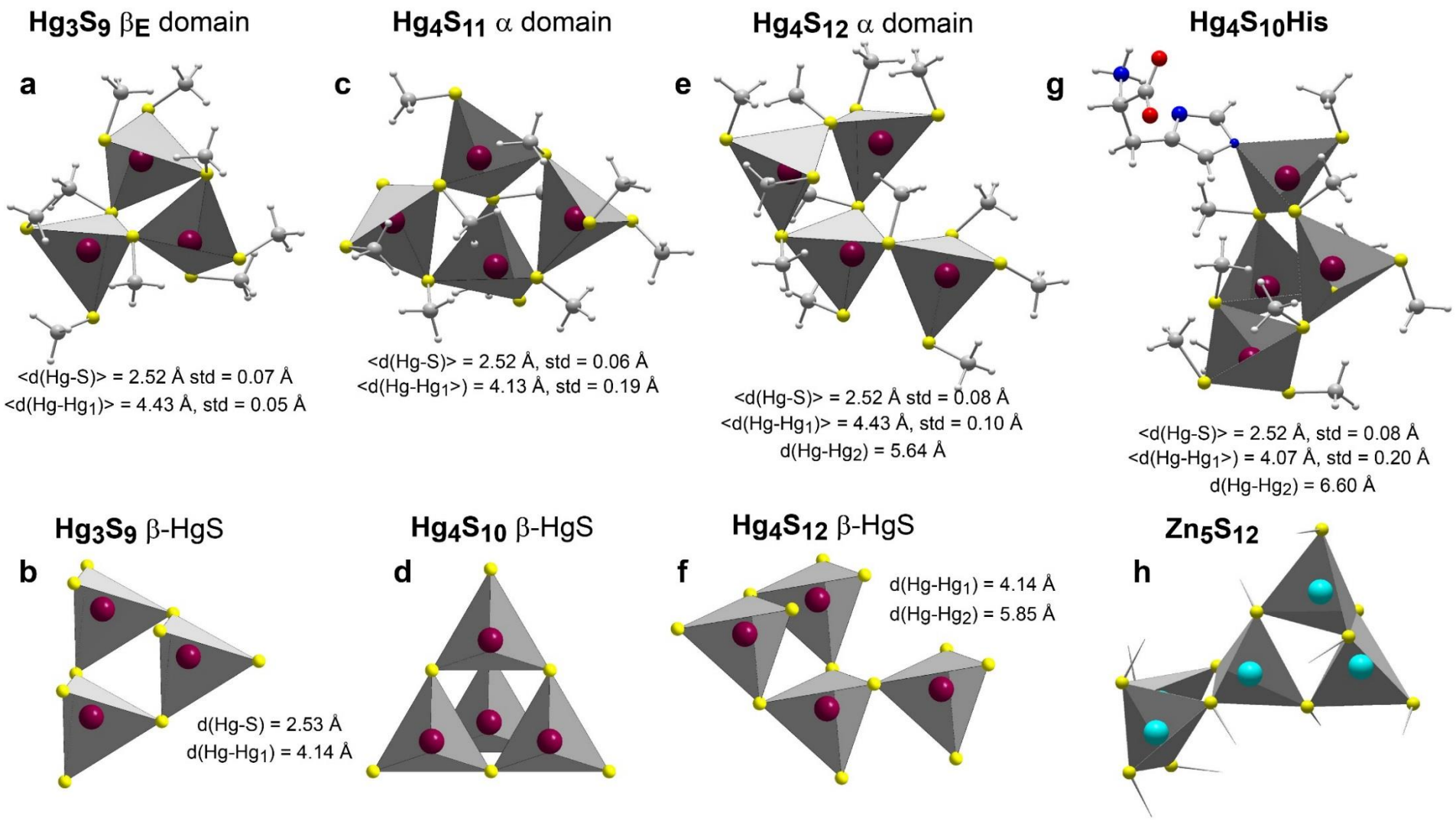

Figure 7

Please, print to fit the width of two columns, thank you

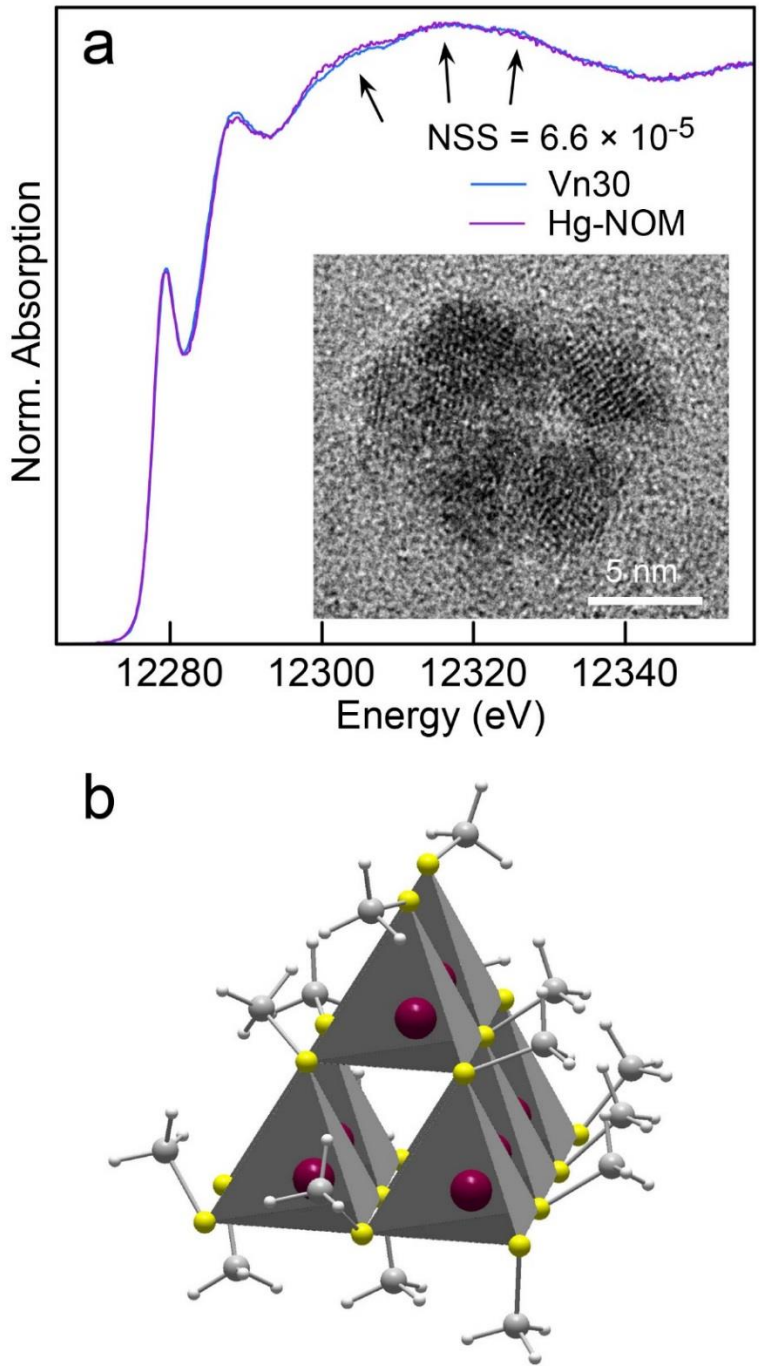

Figure 8

Please, print to fit the width of one column, thank you